bioRxiv preprint doi: https://doi.org/10.1101/2020.12.22.423985; this version posted December 22, 2020. The copyright holder for this preprint (which was not certified by peer review) is the author/funder, who has granted bioRxiv a license to display the preprint in perpetuity. It is made available under aCC-BY 4.0 International license.

CRISPR-based functional genomics in human dendritic cells

Marco Jost[1-4,#], Amy N. Jacobson[5,6,#], Jeffrey A. Hussmann[1-4,8], Giana Cirolia[7], Michael A. Fischbach[5-7,*], Jonathan S. Weissman[1-3,8,9,*]

[1]Department of Cellular and Molecular Pharmacology, University of California, San Francisco, San Francisco, California, USA.

[2]Howard Hughes Medical Institute, University of California, San Francisco, San Francisco, California, USA.

[3]California Institute for Quantitative Biosciences, University of California, San Francisco, San Francisco, California, USA

[4]Department of Microbiology and Immunology, University of California, San Francisco, San Francisco, California, USA.

[5]Department of Bioengineering, Stanford University, Stanford, California, USA

[6]ChEM-H, Stanford University, Stanford, California, USA

[7]Chan Zuckerberg Biohub, San Francisco, California, USA

[8]Whitehead Institute for Biomedical Research, Cambridge, Massachusetts, USA

[9]Department of Biology, Massachusetts Institute of Technology, Cambridge, Massachusetts, USA

[#] These authors contributed equally

* Correspondence should be addressed to: weissman@wi.mit.edu (JSW), fischbach@fischbachgroup.org (MAF)

bioRxiv preprint doi: https://doi.org/10.1101/2020.12.22.423985; this version posted December 22, 2020. The copyright holder for this preprint (which was not certified by peer review) is the author/funder, who has granted bioRxiv a license to display the preprint in perpetuity. It is made available under aCC-BY 4.0 International license.

Abstract

Dendritic cells (DCs) regulate processes ranging from antitumor and antiviral immunity to host-microbe communication at mucosal surfaces. It remains difficult, however, to genetically manipulate human DCs, limiting our ability to probe how DCs elicit specific immune responses. Here, we develop a CRISPR/Cas9 genome editing method for human monocyte-derived DCs (moDCs) that mediates knockouts with a median efficiency of >93% across >300 genes. Using this method, we perform genetic screens in moDCs, identifying mechanisms by which DCs tune responses to lipopolysaccharides from the human microbiome. In addition, we reveal donor-specific responses to lipopolysaccharides, underscoring the importance of assessing immune phenotypes in donor-derived cells, and identify genes that control this specificity, highlighting the potential of our method to pinpoint determinants of inter-individual variation in immune responses. Our work sets the stage for a systematic dissection of the immune signaling at the host-microbiome interface and for targeted engineering of DCs for neoantigen vaccination.

bioRxiv preprint doi: https://doi.org/10.1101/2020.12.22.423985; this version posted December 22, 2020. The copyright holder for this preprint (which was not certified by peer review) is the author/funder, who has granted bioRxiv a license to display the preprint in perpetuity. It is made available under aCC-BY 4.0 International license.

Introduction

DCs play an outsized role in orchestrating innate and adaptive immunity: they act as sentinels, detecting invaders and initiating innate immune responses to clear them, and as antigen-presenting cells, initiating adaptive immune responses that are antigen-specific and tailored to the context in which the antigen was detected (Merad et al., 2013; Sun et al., 2020). In this fashion, DCs mediate pathogen clearance, tumor cell killing, and tolerance to microbiome bacteria or dietary antigens. DCs thus play fundamental roles in shaping host-pathogen and host-microbiome interactions and in the etiology of autoimmune disorders and are a major target for efforts to develop new generations of immunotherapies (Wculek et al., 2020).

Dissecting the pathways by which human DCs respond to innate immune stimuli and relay them into adaptive responses, however, has been challenging, due in large part to difficulties in genetically manipulating human DCs. Although approaches for gene repression in human DCs by RNAi have been reported (Song, 2014), RNAi suffers from limited efficacy and specificity, precluding broader implementation (Kaelin, 2012). As a consequence, DC biology is generally studied in mouse models, but mice and humans differ in many aspects of both innate and adaptive immunity, including innate immune receptor repertoires, responses to immune ligands such as lipopolysaccharide (LPS), and developmental pathways of adaptive immune cells (Pulendran and Davis, 2020). One way to address this challenge is to knock out genes in DC precursor populations such as monocytes or stem cells, followed by differentiation into DCs (Freund et al., 2020; Hiatt et al., 2020; Laustsen et al., 2018). These methods, however, require independent differentiation of each knockout population and as a result are susceptible to batch effects and poorly suited for genetic screens. Moreover, they do not permit probing the functions of genes required for DC differentiation and culture. More broadly, both animal and stem cell

bioRxiv preprint doi: https://doi.org/10.1101/2020.12.22.423985; this version posted December 22, 2020. The copyright holder for this preprint (which was not certified by peer review) is the author/funder, who has granted bioRxiv a license to display the preprint in perpetuity. It is made available under aCC-BY 4.0 International license.

models fail to capture inter-individual variation in immune phenotypes (Sanz et al., 2018), which has been observed for example in innate immune responses, autoimmunity, and pathogen susceptibility and has gained particular salience during the Covid-19 pandemic (Lucas et al., 2020; Pereira et al., 2020). Such variation results from a combination of genetic factors and lifelong environmental exposures (e.g., from the microbiome) but it remains challenging to define the causal determinants in the absence of genetic tools for patient-derived immune cells such as DCs.

To address these limitations, we developed a CRISPR/Cas9-based strategy to construct targeted knockouts directly in human monocyte-derived DCs (moDCs), which are readily derived from donor blood and are widely used for research and clinical applications (Sallusto and Lanzavecchia, 1994; Garg et al., 2017). Using this strategy, we conducted a genetic screen for factors that recognize an innate immune ligand from the human microbiome, LPS from the gut commensal *Bacteroides thetaiotaomicron* (*B. theta*), and identified both mechanisms of species-specific LPS recognition and factors that give rise to inter-individual variation in the response to LPS. These results highlight the utility of our strategy in identifying receptors for innate immune ligands, such as those from the human microbiome, and in pinpointing the genetic bases of inter-individual variation in human immunity. More broadly, our work now provides a general blueprint for functional genomics in human DCs and enables targeted DC engineering for deployment in immunotherapy.

bioRxiv preprint doi: https://doi.org/10.1101/2020.12.22.423985; this version posted December 22, 2020. The copyright holder for this preprint (which was not certified by peer review) is the author/funder, who has granted bioRxiv a license to display the preprint in perpetuity. It is made available under aCC-BY 4.0 International license.

Results

A CRISPR/Cas9 strategy for functional genomics in moDCs

To enable introduction of specific knockouts in moDCs, we developed a non-viral genome editing strategy based on electroporation of *in vitro*-assembled Cas9-sgRNA complexes (Cas9 ribonucleoprotein particles, RNPs), an approach that has been validated in other immune cell types (Freund et al., 2020; Hiatt et al., 2020; Riggan et al., 2020; Roth et al., 2018; Schumann et al., 2015). Briefly, our strategy entails isolating monocytes from human donor blood, differentiating them into moDCs in the presence of GM-CSF and IL-4, and electroporating these moDCs with Cas9 RNPs to induce double-strand breaks at the targeted locus (Figure 1a). Such double-strand breaks trigger error-prone DNA repair and subsequent formation of insertions or deletions (indels) that, with a certain frequency, cause frameshift mutations and thus knockout of the targeted gene. We monitor the efficiency of this process by genotyping using next-generation sequencing and by phenotyping using functional assays.

We first electroporated moDCs with Cas9 RNPs targeting *AAVS1*, using a validated sgRNA sequence (Mali et al., 2013), as well as *TNF* and *TLR4* with sgRNA sequences from the Brunello library (Supplementary File 1) (Doench et al., 2016). By testing a grid of electroporation conditions, we identified conditions with efficient genome editing of *AAVS1* and *TNF* and limited toxicity, but editing of *TLR4* was inefficient (Figure 1b-c, Figure 1 – Figure Supplement 1a-b, Supplementary File 2). The large majority of observed indels were 1- or 2-bp deletions (Figure 1d, Figure 1 – Figure Supplement 1c), which are frameshift mutations that eliminate the function of the gene.

To improve editing efficiency, we i) leveraged sgRNA design tools optimized for RNP activity (CRISPR Design Tool, Synthego) and ii) targeted each locus with 2-3 sgRNAs with

bioRxiv preprint doi: https://doi.org/10.1101/2020.12.22.423985; this version posted December 22, 2020. The copyright holder for this preprint (which was not certified by peer review) is the author/funder, who has granted bioRxiv a license to display the preprint in perpetuity. It is made available under aCC-BY 4.0 International license.

binding sites tiled across a 200-bp stretch to induce simultaneous double-strand breaks, a design that increases the likelihood of achieving functional knockouts by preventing error-free DNA repair and/or removing a stretch of the gene (Methods) (Riggan et al., 2020). Because such large deletions generate smaller amplicons in our genotyping approach, which may be overrepresented in sequencing counts due to length biases in PCR amplification and the sequencing reaction itself, we devised a scheme to correct sequencing counts for length differences to the WT locus to accurately quantify editing efficiency (Figure 1 – Figure Supplement 2, Methods). Testing the multi-sgRNA approach across three loci revealed a shift in indel profiles toward large deletions and multiple indels with deletions of sequences between sgRNA cut sites as well as a modest increase in editing efficiency (Figure 1e, Figure 1 – Figure Supplement 1d-e). Cas9 RNPs assembled with sgRNAs rather than with crRNA:tracrRNA duplexes mediated higher editing efficiency (Figure 1 – Figure Supplement 1d). Through an expansive grid search of electroporation conditions, we next identified a condition (P3, DJ108) with editing efficiencies >90%, high cell recovery, and high specificity in detecting loss of TNF-α secretion upon stimulation with LPS from *E. coli* O55 (*E. coli* LPS) after knockout of *TNF* or the LPS receptor *TLR4* (Poltorak et al., 1998) but not *CXCR4*, a chemokine receptor not involved in LPS signaling (Figure 1 – Figure Supplement 3a). We used this condition for all further experiments, although other conditions also permitted efficient genome editing (Figure 1 – Figure Supplement 3a). Benchmarking the procedure for 10 genes in moDCs derived from three independent donors revealed editing efficiencies >80% for all genes and >90% for most genes (Figure 1f, Figure 1 – Figure Supplement 3b).

In parallel, we challenged knockout moDCs from two donors with *E. coli* LPS, a TLR4 agonist, and measured production of two cytokines: i) TNF-α, which is induced by MYD88 and

bioRxiv preprint doi: https://doi.org/10.1101/2020.12.22.423985; this version posted December 22, 2020. The copyright holder for this preprint (which was not certified by peer review) is the author/funder, who has granted bioRxiv a license to display the preprint in perpetuity. It is made available under aCC-BY 4.0 International license.

TRIF (*TICAM1*) downstream of TLR4, and ii) CXCL10 (IP-10), which is induced solely by TRIF via activation of IRF3 and production of interferon beta (*IFNB1*) (Fitzgerald et al., 2003; Fitzgerald and Kagan, 2020; Yamamoto et al., 2003, 2002). We normalized cytokine production for each knockout population to that from moDCs with knockout of *RPE65*, a retinal pigment epithelium-specific gene that does not contribute to DC function and serves as a neutral control. *TLR4* knockout abolished production of both TNF-α and CXCL10, knockout of *MYD88* or *TNF* reduced TNF-α production (and mildly increased CXCL10 production in at least one donor), *TICAM1* knockout strongly reduced CXCL10 production and moderately reduced TNF-α production, and knockout of *IFNB1* or *IRF3* only reduced CXCL10 production (Figure 1, Figure 1 – Figure Supplement 3c). The effect of knocking out *IRF3* was weak, perhaps due to redundancy with other transcription factors such as *IRF7* or due to incomplete protein depletion. Separately, knockout moDCs from an independent donor challenged with *E. coli* LPS or Pam3CSK4, a TLR2/TLR1 agonist, responded as expected: knockout of *TNF* or *MYD88* reduced the response to both stimuli, whereas knockout of *TLR4* or *TLR2* only reduced the responses to their cognate ligands (Figure 1 – Figure Supplement 3b). Thus, our moDC genome editing strategy enables the detection of functional consequences of knockouts, demonstrating that we can effect protein depletion without perturbing the ability of moDCs to respond to innate immune stimuli.

DC responses to LPSs are specific to bacterial species and vary across indviduals

We next sought to apply our genome editing strategy to answer a central question in innate immunity. Despite LPS being a classic inflammatory molecule, humans are colonized by trillions of Gram-negative microbes that generate milligram to gram quantities of LPS in their intestinal

bioRxiv preprint doi: https://doi.org/10.1101/2020.12.22.423985; this version posted December 22, 2020. The copyright holder for this preprint (which was not certified by peer review) is the author/funder, who has granted bioRxiv a license to display the preprint in perpetuity. It is made available under aCC-BY 4.0 International license.

tracts without tonic inflammation. This observation has been attributed in part to the different chemical structures and immunomodulatory activities of LPSs from commensal Bacteroidetes, among the most common Gram-negative phyla in the guts of Western individuals (Wexler and Goodman, 2017), compared to the canonical inflammatory LPSs from *E. coli* and related Proteobacteria (Coats et al., 2011; Tan et al., 2015; Vatanen et al., 2016; d'Hennezel et al., 2017). Indeed, the Bacteroidetes-to-Proteobacteria LPS ratio in the gut microbiome has been associated with the incidence of type 1 diabetes (Vatanen et al., 2016), suggesting that LPSs from the human microbiome contribute to shaping immune function. The biological activities of LPSs from gut Bacteroidetes, however, have remained controversial as they have been reported to be both TLR4 antagonists and agonists (d'Hennezel et al., 2017; Steimle et al., 2019; Vatanen et al., 2016). We set out to establish how human DCs respond to LPS from Bacteroidetes and more broadly how DCs discriminate different LPSs and initiate specific immune responses.

We focused on LPS from *B. theta*, an abundant member of the human gut microbiota whose LPS biosynthetic machinery has been characterized, allowing us to genetically manipulate its structure (Coats et al., 2011; Cullen et al., 2015; Jacobson et al., 2018). (*B. theta* LPS formally is a lipoooligosaccharide, but we refer to it as LPS for clarity.) We purified LPS from a *B. theta* strain carrying deletions of all eight capsular polysaccharide biosynthetic gene clusters (Porter et al., 2017) to obtain LPS without other contaminating glycolipids. Human moDCs stimulated with *B. theta* LPS secreted moderate levels of TNF-α as quantified by ELISA; this response was weaker than that elicited by *E. coli* LPS both in magnitude and apparent EC_{50} but substantially stronger than that elicited by *Rhodobacter sphaeroides* LPS, a well-characterized TLR4 antagonist (Figure 2a) (Golenbock et al., 1991). Although the pattern was consistent across moDCs from independent donors, response magnitude and EC_{50} varied by 6-fold and >20-fold,

bioRxiv preprint doi: https://doi.org/10.1101/2020.12.22.423985; this version posted December 22, 2020. The copyright holder for this preprint (which was not certified by peer review) is the author/funder, who has granted bioRxiv a license to display the preprint in perpetuity. It is made available under aCC-BY 4.0 International license.

176 respectively (Figure 2 – Figure Supplement 1a), even for moDCs processed in parallel,
177 suggesting that donor-specific factors shape immune responses. Analysis of the transcriptional
178 responses of moDCs by RT-qPCR and RNA-seq confirmed that *B. theta* LPS activated both
179 MYD88 and TRIF signaling more weakly than *E. coli* LPS, with a more pronounced difference
180 for TRIF signaling, again with donor-to-donor variation (Figure 2b, Figure 2 – Figure
181 Supplement 1b-c).
182 To further establish if *B. theta* LPS is a mild agonist of TLR4 rather than an antagonist,
183 we turned to genetic engineering of *B. theta* LPS. LPSs of Bacteroidetes generally contain
184 pentaacylated, monophosphorylated lipid A as opposed to the hexaacylated, diphosphorylated
185 lipid A of Proteobacteria (Coats et al., 2011; Weintraub et al., 1989), in addition to other
186 differences including lipid A acyl group structures and LPS glycan composition. A previous
187 study had established that *B. theta* LPS modified to contain pentaacylated, diphosphorylated lipid
188 A has increased capacity to stimulate TLR4 signaling via the endocytotic pathway (Tan et al.,
189 2015). Hypothesizing that *B. theta* lipid A further lacking an acyl group would resemble known
190 TLR4 antagonists (Golenbock et al., 1991) and thus have decreased immunostimulatory activity,
191 we stimulated moDCs with LPS purified from a *B. theta* strain genetically engineered to produce
192 tetraacylated, diphosphorylated lipid A (*B. theta* 4PP LPS) (Jacobson et al., 2018). *B. theta* 4PP
193 LPS elicited substantially lower levels of TNF-α production and smaller transcriptional
194 responses than *B. theta* WT LPS, with barely detectable responses in some donors (Figure 2a-b,
195 Figure 2 – Figure Supplement 1c). Thus, *B. theta* LPS is a mild TLR4 agonist whose
196 immunostimulatory activity can be tuned by rational engineering.
197
198

bioRxiv preprint doi: https://doi.org/10.1101/2020.12.22.423985; this version posted December 22, 2020. The copyright holder for this preprint (which was not certified by peer review) is the author/funder, who has granted bioRxiv a license to display the preprint in perpetuity. It is made available under aCC-BY 4.0 International license.

A genetic screen identifies receptors for B. theta LPS and drivers of inter-individual variation

To determine if the difference in activity between *B. theta* LPS and *E. coli* LPS arises solely from different capacity to activate TLR4, we tested how *TLR4* knockout affects responses to these two LPSs. *TLR4* knockout moDCs did not secrete detectable amounts of TNF-α in response to *E. coli* LPS but secreted substantial amounts of TNF-α in response to *B. theta* LPS, corresponding to 30-50% of the levels secreted by moDCs with knockout of the neutral control gene *RPE65* (Figure 2 – Figure Supplement 2a-c). Similarly, *TLR4* knockout moDCs retained a partial transcriptional response to *B. theta* LPS corresponding to activation of MYD88, but not TRIF (Figure 2 – Figure Supplement 2d-f). These results suggested that receptors other than TLR4 contribute to recognition of *B. theta* LPS.

To identify such additional receptors, we leveraged our moDC editing strategy to conduct an arrayed genetic screen (Figure 3a). We designed a focused library targeting ~300 genes including known and predicted pattern recognition receptors and multiple nodes of signaling pathways downstream of each receptor class (Methods). We targeted each gene with 2-3 sgRNAs whenever multiple unique sgRNAs could be designed, distributed over four 96-well plates, each of which also included four types of controls (Figure 3 – Figure Supplement 1, Methods). After electroporating moDCs from two independent donors with this library, we assayed editing efficiency and TNF-α secretion in response to 100 ng/mL *B. theta* LPS (Methods, Supplementary Files 3, 4). Editing efficiency was high in both donors, with median efficiencies of 93% and 97.6% (Figure 3b, Figure 3 – Figure Supplement 2-4). TNF-α secretion in response to *B. theta* LPS was strongly reduced by knockouts in the TLR4 signaling pathway, including *TLR4* and its co-receptor MD2 (*LY96*), *CD14* (which delivers LPS to TLR4 and initiates TLR4 endocytosis (Zanoni et al., 2011)), as well as genes involved in MYD88 signaling,

bioRxiv preprint doi: https://doi.org/10.1101/2020.12.22.423985; this version posted December 22, 2020. The copyright holder for this preprint (which was not certified by peer review) is the author/funder, who has granted bioRxiv a license to display the preprint in perpetuity. It is made available under aCC-BY 4.0 International license.

the branch of TRIF signaling involved in NF-κB activation, and the NF-κB factor *RELA* (Figure 3c, Figure 3 – Figure Supplement 5a-c). Indeed, 8-9 of the 10 targeted genes in MYD88 signaling reduced TNF-α secretion for both donors. Other knockouts also caused expected phenotypes; for example, moDCs with knockout of A20 (*TNFAIP3*), which inhibits LPS- and TNF-α-induced NF-κB signaling, secreted more TNF-α (Figure 3c, Figure 3 – Figure Supplement 5c). Thus, our genetic screen accurately captured the genetic requirements for the response to *B. theta* LPS.

Although the results for the two donors were similar overall, we noticed several key differences. Most prominently, knockouts of *PTPN6* (SHP-1) and to a lesser extent *IL10* increased TNF-α secretion in response to *B. theta* LPS in one donor ("donor i") but not the other ("donor h"), suggesting that these factors can constitutively suppress TNF-α secretion in a manner that differs among individuals (Figure 3d). Indeed, unedited moDCs from donor i secreted less TNF-α in response to both *B. theta* LPS and *E. coli* LPS than those from donor h (Figure 3e). Second, MYD88 signaling contributed particularly strongly to the response to *B. theta* LPS for donor h: knockout of *TIRAP*, the TLR4-proximal adapter for MYD88 signaling (Fitzgerald et al., 2001; Fitzgerald and Kagan, 2020), induced the strongest decrease in TNF-α secretion other than *TNF* itself. For donor i, *TLR4* and the TRIF pathway contributed more strongly to the response, as evidenced by strong decreases in TNF-α secretion upon knockout of *TLR4* alone, TRAM (*TICAM2*), and TRIF (*TICAM1*) (Figure 3c-d). A separate 40-gene validation experiment with cells from two additional, independent donors recapitulated these results, with results from each of the two validation donors aligning more closely with those from one of the initial donors (Figure 3 – Figure Supplement 6).

bioRxiv preprint doi: https://doi.org/10.1101/2020.12.22.423985; this version posted December 22, 2020. The copyright holder for this preprint (which was not certified by peer review) is the author/funder, who has granted bioRxiv a license to display the preprint in perpetuity. It is made available under aCC-BY 4.0 International license.

We further investigated two specific observations. First, because *TIRAP* knockout caused a larger decrease in TNF-α secretion than *TLR4* knockout in donor h, we wondered if other TLRs contributed to the response to *B. theta* LPS. We focused on TLR2, canonically known as a receptor for lipopeptides and teichoic acids, because *TLR2* knockout caused the next-strongest decrease in TNF-α secretion among TLRs and because TLR2 has been implicated in the response to non-proteobacterial LPSs (Di Lorenzo et al., 2020; Werts et al., 2001), although these claims remain controversial. Indeed, moDCs with simultaneous knockout of *TLR4* and *TLR2* exhibited the strongest decreases in TNF-α secretion among all samples for both donors (Figure 3f, Figure 3 – Figure Supplement 4d). In addition, knockout of *TLR2* alone reduced the response to *B. theta* LPS but not to *E. coli* LPS in a donor in our validation experiment (Figure 3 – Figure Supplement 6b). These results are consistent with the possibility that TLR2 contributes to the response to *B. theta* LPS, although we cannot rule out the presence of contaminating lipopeptides in our LPS preparation.

Second, to analyze the interplay between PTPN6 and IL-10 in suppressing TNF-α secretion in moDCs from donor i, we measured IL-10 levels in the same samples. The effects of knockouts on TNF-α and IL-10 secretion were well-correlated, suggesting that TLR4 signaling via the TRIF and MYD88 branches accounts for secretion of both TNF-α and IL-10. PTPN6 stood out as an exception: whereas *PTPN6* knockout strongly increased TNF-α secretion, it moderately decreased IL-10 secretion (Figure 3g), suggesting either that IL-10 acts upstream of PTPN6 in suppressing TNF-α secretion or that PTPN6 specifically inhibits production of TNF-α and not IL-10. More broadly, these results demonstrate how combining our moDC editing strategy with multiple readouts can increase the resolution in evaluating immune response pathways.

bioRxiv preprint doi: https://doi.org/10.1101/2020.12.22.423985; this version posted December 22, 2020. The copyright holder for this preprint (which was not certified by peer review) is the author/funder, who has granted bioRxiv a license to display the preprint in perpetuity. It is made available under aCC-BY 4.0 International license.

Discussion

In summary, we describe an efficient and flexible strategy to introduce knockouts in DCs derived from human donors. Our strategy is compatible with diverse readouts, such as cytokine profiling, RNA-seq, flow cytometry, and microscopy, and enables genetic screens at previously intractable scales, transforming our ability to probe the roles of DCs in human biology. Using our strategy, we derive three main conclusions regarding the recognition of LPSs from the human microbiome. First, we observe a contribution of TLR2 to signaling by *B. theta* LPS, which could result from either an intrinsic ability of *B. theta* LPS to bind both TLR4 and TLR2 or the presence of contaminating TLR2 ligands in our *B. theta* LPS preparation. Although we cannot rule out contamination, our observation is consistent with a recent report suggesting that *B. vulgatus* LPS binds to TLR2 (Di Lorenzo et al., 2020). Second, moDCs from different donors have distinct responses—both in magnitude and apparent affinity—to identical preparations of LPS, pointing to inter-individual variation in immune responses. Such variation likely results from a combination of genetic factors and environmental exposures that together determine immune cell state, underscoring the importance of probing immune responses directly in donor-derived cells. Third, in *PTPN6*/SHP-1 we identify a specific factor that contributes to this variation, revealing how our approach enables dissecting the genetic bases of such inter-individual variation. Activation of *PTPN6*/SHP-1, in addition to regulating innate immunity, suppresses antigen cross-presentation (Ding et al., 2016), which some pathogens exploit to subvert adaptive immunity (C. Khouili et al., 2020). Our finding of inter-individual variation in *PTPN6*/SHP-1 activity thus has immediate implications both for understanding variations in

bioRxiv preprint doi: https://doi.org/10.1101/2020.12.22.423985; this version posted December 22, 2020. The copyright holder for this preprint (which was not certified by peer review) is the author/funder, who has granted bioRxiv a license to display the preprint in perpetuity. It is made available under aCC-BY 4.0 International license.

pathogen susceptibility and for personalizing DC vaccines aimed at initiating CD8 T-cell responses.

More broadly, we find that human DCs initiate specific responses to LPS from commensal Bacteroidetes, challenging the notion that these LPSs are innocuous components of the human gut microbiota, as further evidenced by a recent report that homeostatic, TLR4-dependent induction of IFN-β by *B. fragilis* LPS contributes to antiviral immunity (Stefan et al., 2020). Variations in LPS structure across gut commensals instead alter capacity to activate TLR4 and may allow for engagement of new receptors altogether, with the potential for neomorphic activities as well as further complexity arising from combinatorial perception (Antebi et al., 2017). In this fashion, commensal LPSs likely contribute to shaping immune responses at the host-microbiome interface. Understanding the underlying mechanisms, using for example the genetic approaches we describe, may in turn enable efforts to engineer LPSs with defined immunomodulatory capacities, akin to our *B. theta* 4PP mutant.

Beyond LPS recognition, the availability of genetic tools for human DCs now opens the door to a range of applications including systematic functional genomics studies to dissect the roles of DC receptors and signaling pathways in mounting immune responses to commensals, pathogens, or tumor cells and targeted engineering of moDCs for therapeutic interventions such as neoantigen vaccination.

bioRxiv preprint doi: https://doi.org/10.1101/2020.12.22.423985; this version posted December 22, 2020. The copyright holder for this preprint (which was not certified by peer review) is the author/funder, who has granted bioRxiv a license to display the preprint in perpetuity. It is made available under aCC-BY 4.0 International license.

Materials and Methods

Reagents

Complete RPMI medium was generated by supplementing RPMI 1640 medium containing 25 mM HEPES, 2 mM L-glutamine, 2 g/L $NaHCO_3$ (Gibco, Dublin, Ireland) with 10% (v/v) standard fetal bovine serum (VWR, Wayne, PA), 100 units/mL penicillin, 100 µg/mL streptomycin, and 2 mM L-glutamine (Gibco). Lyophilized recombinant human GM-CSF (Gemini Bio, Sacramento, CA) and recombinant human IL-4 (Gemini Bio) were reconstituted to 100 µg/mL and 40 µg/mL, respectively, in sterile ddH_2O, aliquoted into 40-100 µL aliquots, and frozen at –30 °C until use. Fluorescently labeled antibodies against human CD14 (clone HCD14, PE-, PerCP-Cy5.5-, or BV421-labeled), CD80 (clone 2D10, APC-labeled), CD83 (clone HB15e, APC-Cy7-labeled), CD86 (clone BU63, FITC- or BV605-labeled), HLA-DR (clone L243, PE- or FITC-labeled), CD11b (clone LM2, PE-Cy7-labeled), CD11c (clone Bu15, FITC- or PerCP-Cy5.5-labeled), and CD205/DEC205 (clone HD30, PE-labeled) were obtained from BioLegend (San Diego, CA). Ultrapure LPS from *E. coli* O55:B5 and *Rhodobacter sphaeroides*, along with Pam3CSK4, were obtained from Invivogen (San Diego, CA). Solid medium used for bacterial growth was BHI/blood agar, made from Brain Heart Infusion Agar (BD Biosciences, San Jose, CA) with 10% defibrinated horse blood (Hemostat Laboratories, Dixon, CA). Liquid medium used for bacterial growth was supplemented BHI broth, made by preparing 1 L Brain Heart Infusion Broth (BD), and immediately before starting cultures adding 1 mL bovine hemin stock (Sigma, St. Louis, MO), 5 mg/mL in 1 N sodium hydroxide and filter sterilized, and 10 mL L-cysteine hydrochloride (Sigma), 50 mg/mL in Milli-Q water and filter sterilized. Sources of sgRNAs and Cas9 are listed below.

bioRxiv preprint doi: https://doi.org/10.1101/2020.12.22.423985; this version posted December 22, 2020. The copyright holder for this preprint (which was not certified by peer review) is the author/funder, who has granted bioRxiv a license to display the preprint in perpetuity. It is made available under aCC-BY 4.0 International license.

Bacterial culture

B. theta strains were stored at –80 °C in growth medium mixed in equal volume with 50% glycerol in water. Strains were streaked from glycerol stocks onto BHI/blood agar using plastic inoculating loops. Strains were allowed to grow 24-48 h in an anaerobic chamber. Single colonies were used to inoculate 4 10-mL aliquots of supplemented BHI broth per strain, and after 24 h the 10-mL cultures were expanded to 1 L each in glass bottles, producing 4 L total culture volume per strain. Cultures were allowed to grow to stationary phase (24-36 h) and were pelleted at 3400 × *g* for 1 h at 4 °C. Pellets were washed in PBS and shipped frozen to the UCSD GlycoAnalytics Core for LPS purification.

B. theta strains

Both the acapsular *B. theta* strain (ΔCPS) and the *B. theta* 4PP strain have been previously reported (Jacobson et al., 2018; Porter et al., 2017). Briefly, the mutants were created using homologous recombination, creating scarless knockouts of the target genes/gene clusters with no remaining antibiotic resistance markers. The acapsular strain has had all known *B. theta* capsular polysaccharide gene clusters deleted (8 clusters in total), and the 4PP strain has had lipid A acyltransferase *BT2152* and lipid A phosphatase *BT1854* deleted in the acapsular background.

LPS purification

B. theta LPS preparations were performed by Biswa P. Choudhury at the UCSD GlycoAnalytics Core. A cell pellet from 4 L confluent culture of each *B. theta* strain was suspended in Milli-Q water and mixed with an equal volume of 90% phenol solution (Sigma, 328111). The suspension was stirred continuously and maintained at 68 °C ± 2 °C for 30 min. After cooling in an ice bath,

bioRxiv preprint doi: https://doi.org/10.1101/2020.12.22.423985; this version posted December 22, 2020. The copyright holder for this preprint (which was not certified by peer review) is the author/funder, who has granted bioRxiv a license to display the preprint in perpetuity. It is made available under aCC-BY 4.0 International license.

suspensions were centrifuged at 3500 rpm at 10 °C for 45 min and the upper layer removed to a clean Falcon tube. The remaining layers were extracted again with an equal volume of water for 30 min, cooled, and centrifuged as before. The upper layers were pooled and dialyzed (1000 MWCO, regenerated cellulose tubing) against 4 L of water for 4 d, replacing the water twice per day. The dialysate was lyophilized, resuspended in water, and subjected to ultracentrifugation at 105,000 × *g* for 4 h. The pellet was resuspended in water, treated with DNase I, RNase A, and proteinase K, followed by another round of ultracentrifugation as above. The resulting pellet was resuspended in water and lyophilized.

Differentiation of monocyte-derived DCs

Human moDCs were differentiated from monocytes isolated from commercially sourced fresh peripheral blood mononuclear cells (PBMCs) from de-identified healthy human donors (AllCells, Alameda, CA). The authors did not obtain identifiable private information on donors. The commercial vendor obtained informed consent from all donors covering all experiments and data reported in this manuscript. Monocytes were isolated from PBMCs by negative magnetic selection using the EasySep human monocyte enrichment kit without CD16 depletion (StemCell) following the manufacturer's instructions and using a Big Easy magnet or Easy 50 magnet (StemCell Technologies, Vancouver, Canada). Enriched monocytes were generally >80% CD14-positive, as assessed by flow cytometry on an LSR-II flow cytometer (BD BioSciences) or an Attune NxT flow cytometer (Thermo Fisher Scientific, Waltham, MA). Cell counts were determined in duplicate using a Countess II automated hemocytometer (Thermo Fisher Scientific). The isolated monocytes were cultured in complete RPMI medium, supplemented with 50 ng/mL GM-CSF and 20 ng/mL IL-4 immediately prior to use, at a density of $1 \cdot 10^6$ to

bioRxiv preprint doi: https://doi.org/10.1101/2020.12.22.423985; this version posted December 22, 2020. The copyright holder for this preprint (which was not certified by peer review) is the author/funder, who has granted bioRxiv a license to display the preprint in perpetuity. It is made available under aCC-BY 4.0 International license.

379 $1.3 \cdot 10^6$ per mL at 37 °C and 5% CO_2 for 7 d. Medium was exchanged every two or three days
380 during this period (twice total). DCs on day 7 were generally positive for CD80, CD83, HLA-
381 DR, CD11b, CD11c, and CD205 and expressed intermediate levels of CD86 and low to
382 intermediate levels of CD14 with some donor-to-donor variation, as assessed by flow cytometry
383 on an LSR-II flow cytometer (BD BioSciences) or an Attune NxT flow cytometer (Thermo
384 Fisher Scientific). All manipulations were performed in polystyrene conical tubes.
385 All experiments reported in this manuscript were conducted using the methods described
386 above. Preliminary experiments were also performed after isolation of monocytes using the
387 EasySep human monocyte enrichment kit with CD16 depletion (StemCell Technologies) and the
388 EasySep human monocyte isolation kit (StemCell Technologies) with equivalent results.
389 Analogous experiments were also performed with cells cultured in RPMI 1640 medium without
390 supplementation of penicillin/ streptomycin/L-glutamine, with equivalent results. RNA-seq data
391 from moDCs from the same donor differentiated in parallel with and without
392 penicillin/streptomycin/L-glutamine were virtually identical (not shown).
393
394 *Harvesting of moDCs*
395 For all assays, both non-attached and loosely attached moDCs were harvested and then
396 combined. The culture supernatant containing the non-attached cells was first transferred to a
397 conical tube. The remaining attached cells were then detached by addition of CellStripper
398 (Corning, Corning, NY), a non-enzymatic dissociation solution, to the flask (3 mL for a T-150
399 flask, 1.5 mL for a T-75 flask, 0.5 mL for a T-25 flask) and incubation at 37 °C and 5% CO_2 for
400 15 min. The cells were further detached by pipetting and gently tapping the flasks. The
401 suspension was aspirated into a new conical tube and another round of detachment with

bioRxiv preprint doi: https://doi.org/10.1101/2020.12.22.423985; this version posted December 22, 2020. The copyright holder for this preprint (which was not certified by peer review) is the author/funder, who has granted bioRxiv a license to display the preprint in perpetuity. It is made available under aCC-BY 4.0 International license.

CellStripper was performed for 5 min. The detached cells were combined, centrifuged at 100 × g for 10 min, resuspended in RPMI medium, and combined with the non-attached cells. Cell counts were determined in duplicate using a Countess II automated hemocytometer (Thermo Fisher Scientific); at least two squares were counted for each replicate. All manipulations were performed in polystyrene conical tubes.

Treatments of moDCs

To prepare moDCs for treatments, an aliquot of cells containing an appropriate cell number was centrifuged at 100 × *g* for 10 min. The cells were resuspended in complete RPMI medium without cytokines. For readout by ELISA, cells were dispensed into flat-bottom 96-well plates in aliquots of 20,000 cells in 200 µL and incubated at 37 °C and 5% CO_2 for 2 – 4 h. Each experiment contained medium-only (no cells) and PBS treatment (unstimulated/no treatment control) negative controls. For subsequent RNA isolation, cells were dispensed into flat-bottom 24-well plates in aliquots of 200,000 to 250,000 cells at $1 \cdot 10^6$ cells · mL^{-1}, as indicated for each experiment, and incubated at 37 °C and 5% CO_2 for 2 – 4 h. To initiate the stimulation, purified LPS or PBS (no treatment control) were added to each well to the final desired concentration. LPS stocks were generally prepared at a 20x concentration such that all wells received an equivalent volume of stimulant.

For readout by ELISA, the cells were incubated with the stimuli at 37 °C and 5% CO_2 for 20 h, at which point the supernatants were transferred into a V-bottom 96-well plate, centrifuged at 3200 × *g* for 10 min to remove residual bacteria and cell debris, transferred to new plates, and frozen at –30 °C in aliquots.

bioRxiv preprint doi: https://doi.org/10.1101/2020.12.22.423985; this version posted December 22, 2020. The copyright holder for this preprint (which was not certified by peer review) is the author/funder, who has granted bioRxiv a license to display the preprint in perpetuity. It is made available under aCC-BY 4.0 International license.

For RNA purifications, the cells were incubated with the stimuli at 37 °C and 5% CO_2 for 2 h. To harvest RNA from treated cells, a 3x volume of TRIzol™ LS reagent (Ambion, Naugatuck, CT) or TRI Reagent® (Zymo Research, Irvine, CA) was added directly to the cells. The suspension was mixed by pipetting to lyse the cells, followed by RNA isolation using the Direct-zol™ RNA Miniprep kit (Zymo Research) including an on-column DNase I digestion step. Purified RNA was quantified using a Qubit Fluorometer (Thermo Fisher Scientific) and stored at –80 °C until use.

Quantification of cytokine concentrations by ELISA

TNF-α concentrations in undiluted or appropriately diluted supernatants were determined by ELISA using the SimpleStep human TNF alpha ELISA kit (abcam, Cambridge, MA), performed following the manufacturer's instructions and with endpoint absorbance measurements at 450 nm on an Infinite M200 Pro plate reader (Tecan, Männedorf, Switzerland). For each experiment, absorbance measurements from wells containing a 2-fold dilution series of purified TNF-α (31.25 pg/mL to 2,000 pg/mL, in duplicate) were used to calculate a calibration curve using a 4-parameter logistic fit, which in turn was used to calculate TNF-α concentrations in all sample wells. Concentrations of CXCL10 and IL-10 were determined equivalently using SimpleStep human IP-10 ELISA kit (abcam) and the SimpleStep human IL-10 ELISA kit (abcam), respectively, following the manufacturer's instructions. When handling multiple 96-well plates simultaneously, plates were staggered in 3 min intervals starting with the last wash step to ensure that incubation times with the development solution and stop solution were constant.

bioRxiv preprint doi: https://doi.org/10.1101/2020.12.22.423985; this version posted December 22, 2020. The copyright holder for this preprint (which was not certified by peer review) is the author/funder, who has granted bioRxiv a license to display the preprint in perpetuity. It is made available under aCC-BY 4.0 International license.

RT-qPCR

To generate cDNA, purified RNA was reverse-transcribed using SuperScript™ III Reverse Transcriptase (Thermo Fisher Scientific) with oligo(dT) primers in the presence of RNaseOUT™ Recombinant Ribonuclease Inhibitor (Thermo Fisher Scientific) or using SuperScript™ IV VILO™ Master Mix (Thermo Fisher Scientific). All reactions in a given experiment were normalized to contain the same amount of RNA (250 ng to 600 ng depending on the experiment). cDNA was diluted 1:10 and stored at –30 °C until use. qPCR was performed using the KAPA SYBR® FAST qPCR Master Mix (Roche, Basel, Switzerland) in 20 µL reactions containing 3 µL diluted cDNA and 200 nM of each primer. Reactions were run on a LightCycler® 480 Instrument (Roche). All reactions were performed in technical triplicates. RT-qPCR primers were chosen as intron-spanning primers, when possible, from the Universal ProbeLibrary (Roche), with the following sequences:

ACTB: GCTACGAGCTGCCTGACG (fw), GGCTGGAAGAGTGCCTCA (rv)

IFNB1: CTTTGCTATTTTCAGACAAGATTCA (fw), GCCAGGAGGTTCTCAACAAT (rv)

TNF: CAGCCTCTTCTCCTTCCTGAT (fw), GCCAGAGGGCTGATTAGAGA (rv)

CXCL10: GAAAGCAGTTAGCAAGGAAAGGT (fw),
GACATATACTCCATGTAGGGAAGTGA (rv)

Preparation of sequencing libraries for RNA-seq and data analysis

RNA-seq libraries were prepared from purified RNA using the Stranded mRNA Prep Ligation kit (Illumina, San Diego, CA) in 96-well format, following the manufacturer's instructions. Input RNA amounts were held constant for all samples for a given donor, between 300 and 600 ng per reaction depending on the experiment. Final libraries were validated and quantified using the

bioRxiv preprint doi: https://doi.org/10.1101/2020.12.22.423985; this version posted December 22, 2020. The copyright holder for this preprint (which was not certified by peer review) is the author/funder, who has granted bioRxiv a license to display the preprint in perpetuity. It is made available under aCC-BY 4.0 International license.

2100 Bioanalyzer (Agilent, Santa Clara, CA) using the High Sensitivity DNA kit (Agilent). Paired-end 100 or paired-end 150 sequencing was performed on a HiSeq 4000 (Illumina). Reads were aligned strand-specifically to the human genome (GRCh38) using the spliced read aligner STAR (Dobin et al., 2013), version 2.6.0, against an index containing features from Gencode release 34. Quantification of gene counts was carried out with featureCounts (Liao et al., 2014), version 1.6.2, using only uniquely mapped reads to the reverse strand. Differential expression analysis was carried out on gene counts using DESeq2 (Love et al., 2014), including only genes with an average count >2 across all conditions. Transcript counts per million were calculated by dividing gene counts by effective transcript length, using transcript length from Gencode annotations and an average fragmenth length of 160 (the expected fragment size from the kit and consistent with estimates determined by Kallisto (Bray et al., 2016)), followed by normalization to total transcript counts. All other analyses were performed in python3.6.

sgRNA sequences

For initial experiments, an sgRNA sequence for *AAVS1* was chosen from a previous report (Mali et al., 2013) and sgRNA sequences for *TNF* and *TLR4* were chosen as the top predicted guides from the Brunello library (Doench et al., 2016). All other sgRNAs were purchased from or provided by Synthego (Menlo Park, CA), designed according to their multi-guide RNA strategy (Stoner et al., 2019). Briefly, two or three sgRNAs are bioinformatically designed to work in a cooperative manner to generate small, knockout-causing, fragment deletions in early exons. These fragment deletions are larger than standard indels generated from single guides. The genomic repair patterns from a multi-guide approach are highly predictable based on the guide-spacing and design constraints to limit off-targets, resulting in a higher probability protein

bioRxiv preprint doi: https://doi.org/10.1101/2020.12.22.423985; this version posted December 22, 2020. The copyright holder for this preprint (which was not certified by peer review) is the author/funder, who has granted bioRxiv a license to display the preprint in perpetuity. It is made available under aCC-BY 4.0 International license.

493 knockout phenotype. For the genetic screen, a Pattern Recognition Receptors and Signaling
494 Pathway arrayed library was provided by Synthego. All sgRNA sequences used in this
495 manuscript are listed in Supplementary File 1.
496
497 *RNP assembly*
498 RNPs were assembled by complexing purified recombinant Cas9 from *Streptococcus pyogenes*
499 (Synthego) with chemically synthesized sgRNAs (Synthego). Lyophilized sgRNAs targeting
500 each gene (individual or multiple sgRNAs) were resuspended to 100 µM (total sgRNA
501 concentration) in RNase-free TE buffer (10 mM Tris, 1 mM EDTA, pH 8) for 15 min at 25 °C or
502 over night at 4 °C with intermittent vortexing. Prior to use, sgRNA stocks were diluted to 25 µM
503 in RNase-free H_2O. Both stocks were stored at –30 °C and freeze-thawed up to 5 times. To
504 assemble RNP for electroporation of $4 \cdot 10^5$ cells, 50 pmol sgRNA and 20 pmol Cas9 were
505 combined and diluted to 20 µL with nucleofection solution P1 or P3 (with supplement added,
506 Lonza, Basel, Switzerland). The mixture was incubated at 25 °C for 10 min or up to 2 h and
507 immediately used to electroporate moDCs. For double knockouts, 50 pmol of sgRNA against
508 each gene and 40 pmol Cas9 were combined in a total volume of 23 µL.
509 For experiments with guide RNAs in the crRNA:tracrRNA format (Figure 1 – Figure
510 Supplement 1d), lyophilized crRNAs and tracrRNA (Integrated DNA Technologies, Coralville,
511 Iowa) were resuspended to 400 µM and 100 µM, respectively, in RNase-free TE buffer.
512 crRNA:tracrRNA duplexes were generated by mixing equimolar amounts of crRNA and
513 tracrRNA at a final concentration of 50 µM each, incubating the mixture at 95 °C for 5 min, and
514 allowing the mixture to cool to room temperature on the benchtop. To assemble RNP for
515 electroporation of $4 \cdot 10^5$ cells, 50 pmol crRNA:tracrRNA duplex and 20 pmol Cas9 v3

bioRxiv preprint doi: https://doi.org/10.1101/2020.12.22.423985; this version posted December 22, 2020. The copyright holder for this preprint (which was not certified by peer review) is the author/funder, who has granted bioRxiv a license to display the preprint in perpetuity. It is made available under aCC-BY 4.0 International license.

(Integrated DNA Technologies, stock diluted to 20 µM in sterile PBS) were combined and diluted to 5 µL in PBS, following the manufacturer's instructions.

moDC genome editing by electroporation of Cas9 RNPs

Genome editing was performed by electroporation of moDCs with pre-formed Cas9 RNPs. moDCs were detached as described above. A suspension containing an appropriate number of moDCs ($4 \cdot 10^5$ cells per electroporation + 5% excess) was transferred to a new conical tube and centrifuged at 90 × g for 10 min. The cells were resuspended in 1 – 5 mL PBS and centrifuged again at 90 × g for 10 min. For electroporation with RNPs assembled with sgRNAs (all experiments in this paper except for Figure 1 – Figure Supplement 1d, right), the cells were resuspended in 5 µL nucleofection solution P1 or P3 (with supplement added, Lonza) per $4 \cdot 10^5$ cells. Aliquots of $4 \cdot 10^5$ cells were transferred into individual wells of 16-well or 96-well nucleofection cuvettes (Lonza), combined with 20 µL pre-formed RNP or nucleofector solution (no RNP control), and immediately electroporated using pulse code DJ-108 (solution P3) or other pulse codes, as described, using a Nucleofector-4D (Lonza) or a 96-well shuttle (Amaxa/Lonza) attached to a Nuclefector-4D. For electroporation with RNPs assembled with crRNA:tracrRNA duplexes Figure 1 – Figure Supplement 1d, right), the cells were resuspended in 20 µL nucleofection solution P1 or P3 (with supplement added, Lonza) per $4 \cdot 10^5$ cells and 5 µL pre-formed RNP or nucleofector solution (no RNP control) was added. Immediately after nucleofection, 75 µL pre-warmed complete RPMI medium supplemented with 50 ng/mL GM-CSF and 20 ng/mL IL-4 were added to each well without disturbing the cells by letting the medium run down the side of the cuvette. After incubation at 37 °C and 5% CO_2 for 1 h, the cells were mixed by pipetting and then split into 2 wells of a flat-bottom 96-well plate filled with 50

bioRxiv preprint doi: https://doi.org/10.1101/2020.12.22.423985; this version posted December 22, 2020. The copyright holder for this preprint (which was not certified by peer review) is the author/funder, who has granted bioRxiv a license to display the preprint in perpetuity. It is made available under aCC-BY 4.0 International license.

539 µL pre-warmed complete RPMI medium supplemented with 50 ng/mL GM-CSF and 20 ng/mL
540 IL-4. The cells were incubated at 37 °C and 5% CO_2 for 5 d, with medium replenished after 2 or
541 3 d and then used for assays.

542 The final electroporation condition (solution P3, pulse code DJ-108, $4 \cdot 10^5$ cells
543 electroporated with 10 pmol Cas9 and 25 pmol sgRNA) was obtained through iterative grid
544 searches of different conditions. In the process, several other conditions were also found to yield
545 good results, including nucleofection solution P1 with pulse code CB-128 (Figure 1 – Figure
546 Supplement 3a). In initial experiments, we also used solution P1 with pulse code CB-150 (Figure
547 1c, Figure 1 – Figure Supplement 1). Reducing the amount of Cas9 RNP led to a reduction in
548 editing efficiency.

549

550 *Phenotyping of edited moDCs and DNA extraction*

551 For all experiments in this manuscript, electroporated moDCs were harvested for phenotyping
552 and genotyping 5 d post-electroporation, with the exception of data presented in Figure 1 –
553 Figure Supplement 1a, for which some moDCs were harvested 3 d post-electroporation. Both
554 non-attached and attached cells were harvested and then combined, largely as described above.
555 Briefly, the culture supernatants containing non-attached cells were first transferred to V-bottom
556 96-well plates. The remaining attached cells were then detached by addition of 25 µL
557 CellStripper solution (Corning) per well and incubation at 37 °C and 5% CO_2 for 15 min. The
558 cells were further detached by gentle pipetting and tapping of the plate and the suspension was
559 combined with the cell supernatant. Another round of detachment with CellStripper was
560 performed for 5 min and the suspension was combined with the suspension containing the
561 remaining cells. The cells suspensions were centrifuged at 100 × g for 10 min and resuspended in

bioRxiv preprint doi: https://doi.org/10.1101/2020.12.22.423985; this version posted December 22, 2020. The copyright holder for this preprint (which was not certified by peer review) is the author/funder, who has granted bioRxiv a license to display the preprint in perpetuity. It is made available under aCC-BY 4.0 International license.

562 100 µL complete RPMI medium without cytokines. Cells with the same knockout were
563 combined (cells from each electroporation had been split over 2 separate wells of a 96-well
564 plate) and used for phenotyping and genotyping.

565 To determine the responses of cells to stimuli by ELISA, aliquots of cells were
566 transferred into flat bottom 96-well plates, diluted to 200 µL with complete RPMI medium
567 without cytokines, incubated at 37 °C and 5% CO_2 for 2 – 3 h, and stimulated as described
568 above. Each stimulation was performed in duplicate. Supernatants from stimulated cells were
569 harvested and used to measure TNF-α levels as described above.

570 For subsequent RNA isolation, aliquots containing $1 \cdot 10^5$ to $2.5 \cdot 10^5$ cells were
571 transferred into flat-bottom 24-well plates, diluted to 250 µL with complete RPMI medium
572 without cytokines, incubated at 37 °C and 5% CO_2 for 2 – 3 h, and stimulated as described
573 above. Each stimulation was performed in duplicate. RNA was extracted from treated cells as
574 described above.

575 During the incubation prior to stimulation, aliquots of the remaining cell suspension were
576 used to determine cell counts for each sample using a CellTiterGlo luminescence assay
577 (Promega, Madison, WI). Briefly, replicate aliquots of cells were transferred into an opaque flat-
578 bottom 96-well plate, diluted to 100 µL, and incubated at 25 °C for 15 – 30 min. After addition
579 of an equal volume of CellTiterGlo solution to each well, the plates were placed on an orbital
580 shaker for 2 min and then incubated at 25 °C for 10 min. Finally, luminescence in each well was
581 recorded using a GloMax Multi+ luminescence plate reader (Promega). For some experiments,
582 luminescence measurements from wells containing known numbers of unedited moDCs, as
583 determined using a Countess II automated hemocytometer (Thermo Fisher Scientific), were used
584 to calculate cell numbers for each sample. TNF-α secretion for each sample was then normalized

bioRxiv preprint doi: https://doi.org/10.1101/2020.12.22.423985; this version posted December 22, 2020. The copyright holder for this preprint (which was not certified by peer review) is the author/funder, who has granted bioRxiv a license to display the preprint in perpetuity. It is made available under aCC-BY 4.0 International license.

585 to cell numbers. For other experiments, TNF-α secretion was simply normalized to background-
586 subtracted luminescence readings. In benchmark experiments, cell counts were also determined
587 by flow cytometry on an LSR-II flow cytometer (BD Bioscences) equipped with a 96-well
588 autosampler. Cell counts determined by flow cytometry and luminescence were well-correlated
589 (Figure 1 – Figure Supplement 1a) and all further cell counts were determined by luminscence.
590 To isolate genomic DNA from each sample for genotyping, aliquots of harvested moDCs
591 were transferred to a 96-well V-bottom plate, centrifuged at 300 × g for 10 min, and resuspended
592 in 50 µL QuickExtract DNA extraction solution (LuciGen, Middleton, WI). The suspensions
593 were transferred to 96-well PCR plates and incubated at 65 °C for 20 min and then at 98 °C for 5
594 min using a thermocycler. The extracted genomic DNA was stored at –30 °C until use.
595
596 *Genotyping of edited DCs (measurements of editing outcomes)*
597 Genomic regions surrounding each cut site were PCR-amplified using a 2-step protocol, largely
598 as described (Leenay et al., 2019). Briefly, primer pairs were designed for each cut site using
599 Primer-BLAST (Ye et al., 2012) to amplify a 200- to 450-base pair region, ensuring that all cut
600 sites targeted by the pooled sgRNAs as well as a 50-base pair flanking region on each side of the
601 cut sites were included, with a targeted T_m of 60 °C. Constant adapters (forward: 5′-
602 CTCTTTCCCTACACGACGCTCTTCCGATCT-3′; reverse: 5′-
603 CTGGAGTTCAGACGTGTGCTCTTCCGATCT-3′) were appended to the designed primer
604 pairs. First-round PCRs of targeted sites were performed in 96-well format using at least 4,000
605 genomic copies for each sample, 0.5 µM of each primer, and Q5 Hot Start High-Fidelity 2x
606 master mix (NEB, Ipswich, MA) and the following protocol: 98 °C for 30 s; 35 cycles of 98 °C
607 for 10 s, 60 °C for 30 s, and 72 °C for 30 s; and a final extension at 72 °C for 2 min. Products

bioRxiv preprint doi: https://doi.org/10.1101/2020.12.22.423985; this version posted December 22, 2020. The copyright holder for this preprint (which was not certified by peer review) is the author/funder, who has granted bioRxiv a license to display the preprint in perpetuity. It is made available under aCC-BY 4.0 International license.

608 from the first PCR were diluted 1:100 in ddH_2O and subjected to a second round of PCR using
609 the constant adapters as annealing sites, appending Illumina P5 and P7 adapters and two eight-
610 base barcodes on both ends that together uniquely identified each sample. 12 cycles of PCR were
611 performed using the same conditions described above. After the second PCR, all samples were
612 pooled and the combined samples were purified using a 0.8x AMPure XP purification (Beckman
613 Coulter, Brea, CA). Final libraries were validated and quantified using the 2100 Bioanalyzer
614 (Agilent) using the High Sensitivity DNA kit (Agilent) and sequenced in a 600-cycle paired-end
615 run on a MiSeq Instrument (Illumina) using MiSeq v3 Reagent kits.

616 Sequencing data of editing outcomes were analyzed and quantified using knock-knock
617 v0.3 (https://github.com/jeffhussmann/knock-knock) (Canaj et al., 2019). For a few loci, some
618 amplicons contained large deletions with boundaries >20 bp from an sgRNA cut site that were
619 classified as "large deletions" by knock-knock but likely instead reflect amplification of partially
620 complementary fragments, given in particular the rare occurrence of large deletions with
621 individual sgRNAs. To avoid overestimating editing efficiency, reads with at least one alignment
622 boundary >40 bp from an sgRNA cut site or both alignment boundaries >20 bp from sgRNA cut
623 sites were re-classified into the "malformed layout" category. For all experiments in which a
624 gene was targeted with multiple sgRNAs, sequencing counts were adjusted by the size difference
625 to the WT locus, using the following formula:

626 $$count_{corr} = count * 2^{-0.014356*(l_{WT}-l_{read})}$$

627 where count is the raw count, l_{WT} the length in bp of the WT locus, and l_{read} the length in bp of
628 the edited locus. See below for a description of how the coefficient was derived. Results from
629 outcome classification, after correction for size, for all experiments except for the screen are

bioRxiv preprint doi: https://doi.org/10.1101/2020.12.22.423985; this version posted December 22, 2020. The copyright holder for this preprint (which was not certified by peer review) is the author/funder, who has granted bioRxiv a license to display the preprint in perpetuity. It is made available under aCC-BY 4.0 International license.

listed in Supplementary File 2. Results for the screen, after correction for size, are listed in Supplementary File 4.

Empirical assessment of amplicon size bias

To measure how amplicon size affects amplification and sequencing efficiency in our genotyping approach, we subjected pools of purified amplicons of defined sizes to our sequencing library preparation protocol and determined the resulting sequencing counts (Figure 1 – Figure Supplement 2a). Briefly, we designed the strategy based on the following criteria:

1) Amplicons are of defined sizes between ~150 bp and ~500 bp (the range of amplicon sizes in our experiments) and amplified by the same primer pair;
2) Sequencing library preparation protocol is analogous to that used for genotyping, including similar effective template concentration and presence of excess non-productive genomic DNA;
3) Amplicon abundance is measured before sequencing library preparation and compared to final sequencing counts to estimate amplification and sequencing efficiency.

Briefly, we generated five amplicons with final lengths of 146 bp, 249 bp, 349 bp, 447 bp, and 539 bp and with constant annealing sites at the ends by PCR-amplifying different fragments of a gene encoding BFP with a constant forward primer and reverse primers positioned at the appropriate distances. Forward and reverse primers contained overhangs (identical for all reverse primers) to create annealing sites for sequencing library preparation. Following the PCR, each individual amplicon was gel-purified and quantified using a Qubit Fluorometer (Thermo Fisher Scientific). The five amplicons were then mixed into pools at 11 different molar ratios. For increased accuracy, the abundance of each fragment in these pools was measured using the 2100

bioRxiv preprint doi: https://doi.org/10.1101/2020.12.22.423985; this version posted December 22, 2020. The copyright holder for this preprint (which was not certified by peer review) is the author/funder, who has granted bioRxiv a license to display the preprint in perpetuity. It is made available under aCC-BY 4.0 International license.

Bioanalyzer (Agilent) using the High Sensitivity DNA kit (Agilent). Each pool was then diluted to 33 fM (about 20,000 template molecules per µL, equivalent to genomic DNA isolated from 10,000 cells) and 1 µL of diluted pool was used as template for the first-round PCR as described above, using a primer pair complementary to the constant overhangs on each fragment, designed with the same criteria as our other amplicon primers. The PCRs additionally contained 4 µL of genomic DNA from unedited DCs as excess non-productive template. The remainder of the sequencing library preparation was carried out as described above, with unique sequencing indices appended to each pool in the second-round PCR. The final libraries were sequenced on a MiSeq (Illumina) and counts for each fragment were determined by aligning reads to the expected amplicons.

To infer observation efficiency (amplification + sequencing) for each fragment, we reasoned that the starting and the final composition of the pool should be related by the specific observation efficiency of each amplicon, which should shift the abundance of each fragment based on its specific observation efficiency:

$$m_i = \frac{e_i s_i}{\sum_{j=1}^{n} e_j s_j}$$

where m_i is the measured fractional abundance, s_i the starting abundance, and e_i the fragment-specific observation efficiency. Note that the equation takes this form because we can measure only fractional rather than absolute abundances of each amplicon at the end; thus

$$\sum_{j=1}^{n} m_j = 1$$

To compute the efficiencies, we arbitrarily set the efficiency e of the 447 bp fragment (which was included in all pools) to 1 ($e_n = 1$) and then solved the resulting linear equation system

$$m_i \sum_{j=1}^{n} e_j s_j = e_i s_i$$

bioRxiv preprint doi: https://doi.org/10.1101/2020.12.22.423985; this version posted December 22, 2020. The copyright holder for this preprint (which was not certified by peer review) is the author/funder, who has granted bioRxiv a license to display the preprint in perpetuity. It is made available under aCC-BY 4.0 International license.

675 $$(m_i - 1)e_i s_i + m_i \sum_{j \neq i}^{n-1} e_j s_j = -m_i s_n$$

676 to obtain the observation efficiencies (amplification + sequencing) e_i for each fragment in each
677 pool. Because we expected per-cycle PCR amplification efficiency to be a major contributor to
678 these efficiencies, we compared $\log_2$ e to fragment size and found it to be linearly correlated
679 (Figure 1 – Figure Supplement 2b). We therefore estimated the contribution of each bp in size
680 difference to observation efficiency using a linear regression of $\log_2$ e against length in bp; we
681 used the slope of this regression to correct sequencing counts as described above. We note that
682 size bias appears to be less evident when small amplicons are already overrepresented in the
683 input (Figure 1 – Figure Supplement 2b), perhaps because under these conditions primers rather
684 than nucleotides are the limiting component in PCR. Because our editing efficiencies are
685 generally high and thus smaller fragments are more abundant at the outset than longer fragments,
686 our correction approach is (intentionally) conservative and should not cause us to overestimate
687 editing efficiency.
688
689 *RNA-seq of edited cells*
690 RNA-seq libraries were prepared from purified RNA as described above. Input RNA amounts
691 were held constant for all samples for a given donor (250 ng for donor p and 400 ng for donor q).
692 For donor p, the RNA extraction for one replicate sample with knockout of *RPE65* and treated
693 with 100 ng/mL *B. theta* LPS failed. Reads were aligned strand-specifically to the human
694 genome, gene counts were quantified, and differential gene expression analysis was conducted as
695 described above. Read coverage along transcripts was quantified using plastid (Dunn and
696 Weissman, 2016). All other analyses were performed in python3.6.
697

bioRxiv preprint doi: https://doi.org/10.1101/2020.12.22.423985; this version posted December 22, 2020. The copyright holder for this preprint (which was not certified by peer review) is the author/funder, who has granted bioRxiv a license to display the preprint in perpetuity. It is made available under aCC-BY 4.0 International license.

Design of library for arrayed genetic screen

To select genes to target in our arrayed genetic screen, we first included all genes from the following categories of pattern recognition receptors (PRRs): Toll-like receptors, NOD-like receptors, RIG-I-like receptors, C-type lectin receptors, Galectins, and SIGLECs. We then assembled a list of all genes encoding relevant signaling proteins downstream of these PRRs, including immediate adaptor proteins, kinases and ubiquitin ligases, the downstream transcription factors, as well a limited subset of effector cytokines and cytokine receptors. Finally, we completed the gene list with additional genes of interest by surveying our RNA-seq data from human moDCs for expressed potential pattern recognition receptors such as predicted surface/membrane proteins, carbohydrate-binding proteins, and proteins containing a V-set domain using searches for Pfam domains, and by browsing the list of genes with the GO term "innate immune response" that we had not yet included. This process ultimately resulted in a list of >400 genes. To narrow the list down to ~300 genes to enable screening in four 96-well plates, we first eliminated pseudogenes and a few PRR-like genes with well-established functions. We then eliminated many genes involved in linear signaling pathways while ensuring that each pathway was targeted at multiple nodes in the final library. In total, we targeted 291 unique genes of interest.

The library additionally included 4 classes of controls: 1) non-targeting negative controls; 2) neutral controls (targeting negative controls); 3) targeting positive controls; and 4) essential controls. As non-targeting negative controls, we picked non-targeting negative controls #1 and #2 from Synthego. As neutral controls, we selected 9 genes (*CRX*, *KCNV1*, *TRHR*, *LALBA*, *RPE65*, *F13B*, *OR2D2*, *OR51T1*, *TAS2R9*) that are not expressed in moDCs, as assessed by our RNA-seq data and non-essential in any cell type surveyed at the time (from Project Achilles)

bioRxiv preprint doi: https://doi.org/10.1101/2020.12.22.423985; this version posted December 22, 2020. The copyright holder for this preprint (which was not certified by peer review) is the author/funder, who has granted bioRxiv a license to display the preprint in perpetuity. It is made available under aCC-BY 4.0 International license.

(Tsherniak et al., 2017), and for which some functional annotation existed such as tissue-specific activity. These genes include olfactory and taste receptors as well as genes expressed only in specific tissues such as the retinal pigment epithelium or the testes. As a targeting positive control for TNF-α ELISA readout, we included *TNF*. As essential controls, we included the two core essential genes (Hart et al., 2015): *U2AF2* (a splicing factor) and *POLR2A* (a component of RNA polymerase II). In total, we included 14 controls. All sgRNA sequences are listed in Supplementary File 1.

Finally, all selected genes were arrayed into 96-well format, with the following design principles: each of the four 96-well plates contained each of the 14 controls in randomized positions on each plate; column 12 was left empty for no pulse electroporation controls and media-only ELISA controls; the remaining 74 positions on each 96-well plate were randomly filled with sgRNAs targeting genes of interest. The final plate layouts are depicted in Figure 3 – Figure Supplement 1 and listed in Supplementary File 3.

Arrayed genetic screen

The Pattern Recognition Receptors and Signaling Pathway arrayed library targeting all selected genes with up to 3 sgRNAs per gene was provided by Synthego. For a few genes, high homology to other loci precluded selection of 3 unique sgRNAs within a 200-bp window; in those cases 2 or 1 sgRNAs were used. Purified, lyophilized sgRNAs were resuspended to 25 µM in 0.25x TE for 16 h at 4 °C, aliquotted into 96-well plates, and frozen at –80 °C until use.

For each screen, monocytes were isolated from $1.5 \cdot 10^9$ PBMCs (AllCells) from a single healthy human donor and differentiated into moDCs as described above. Differentiated moDCs were electroporated with sgRNAs in 96-well format as described above. Plates were staggered in

bioRxiv preprint doi: https://doi.org/10.1101/2020.12.22.423985; this version posted December 22, 2020. The copyright holder for this preprint (which was not certified by peer review) is the author/funder, who has granted bioRxiv a license to display the preprint in perpetuity. It is made available under aCC-BY 4.0 International license.

744 10 min intervals to minimize the amount of time cells spent in nucleofection solution and the
745 time delay between electroporation and addition of recovery media. On day 3 after
746 electroporation, 4 wells of cells containing no pulse/no RNP control cells were harvested to
747 assess responses of unedited cells to *B. theta* LPS and *E. coli* LPS and to determine an optimal *B.*
748 *theta* LPS concentration for treatment of edited cells (Figure 3e). Maintenance, harvesting, and
749 counting of electroporated moDCs was performed as described above. Plates were staggered for
750 luminescence reads to keep incubation time with the luminescence substrate constant. All cells
751 were treated with 100 ng/mL *B. theta* LPS in a volume of 200 µL. Concentrations of TNF-α and
752 IL-10 in cell supernatants were determined by ELISA as described above. Plates were staggered
753 in 7 min intervals throughout the entire process to keep incubation times constant.

754 Log_2 fold-changes in TNF-α or IL-10 secretion were calculated as follows:

755 1) ELISA absorbance values for each individual sample were background-corrected
756 using absorbance values from media-only wells. For the IL-10 ELISAs, background-
757 corrected absorbance below 0 (recorded for four samples) were assigned the
758 background-corrected absorbance of the sample with the lowest value greater than 0.
759 2) Background-corrected absorbance values were normalized by the average
760 luminescence (average of two replicate measurements) for each cell sample to
761 calculate a cell count-normalized absorbance.
762 3) For each sample, the cell count-normalized absorbance was normalized to the median
763 cell count-normalized absorbance of all 9 neutral targeting controls on the same 96-
764 well plate to calculate a fold-change in TNF-α secretion. Normalization was
765 performed by plate to normalize for any plate effects.

bioRxiv preprint doi: https://doi.org/10.1101/2020.12.22.423985; this version posted December 22, 2020. The copyright holder for this preprint (which was not certified by peer review) is the author/funder, who has granted bioRxiv a license to display the preprint in perpetuity. It is made available under aCC-BY 4.0 International license.

4) Fold-changes were $\log_2$ transformed to calculate $\log_2$ fold-changes in TNF-α secretion.
5) Log_2 fold changes of replicate treatments were averaged to calculate the average $\log_2$ fold change of each knockout population. Normality tests suggested that the $\log_2$ fold-changes were generally normally distributed, rationalizing the averaging of the $\log_2$-transformed values.

Raw and processed ELISA and cell count data are included in Supplementary File 3.

To assess editing efficiency at all loci, amplification primer design and sequencing library preparation were streamlined to increase throughput. A first round of amplification primers was designed using PrimerServer (Zhu et al., 2017), which uses a combination of primer3 and BLAST to predict amplification primers. Design criteria were: 1) amplification of a 200- to 450-base pair region, 2) inclusion of all cut sites targeted by the sgRNAs as well as a 35-base pair flanking region on each side of the cut sites was included, 3) ideal T_m of 60 °C. Design criteria were successively relaxed if no primers matching these criteria were found, up to a maximum amplicon size of 500 base pairs and a minimum flanking distance of 25 base pairs. Primers containing overhangs as described above were ordered in 96-well format matching the sgRNA layout and tested for efficient amplification of the targeted locus by amplifying genomic DNA from unedited moDCs and sequencing the resulting amplicons on a MiSeq (Illumina), as described above. For loci with inefficient amplification or a high fraction of off-target amplicons, as assessed using knock-knock (Canaj et al., 2019, p.), primers were designed using PrimerBLAST (Ye et al., 2012) as described above, and efficient amplification confirmed by sequencing. For some highly homologous locus pairs, such as *SFTPA1*/*SFTPA2* and *LGALS7*/*LGALS7B*, no primers could be designed that ensured completely unique amplification

bioRxiv preprint doi: https://doi.org/10.1101/2020.12.22.423985; this version posted December 22, 2020. The copyright holder for this preprint (which was not certified by peer review) is the author/funder, who has granted bioRxiv a license to display the preprint in perpetuity. It is made available under aCC-BY 4.0 International license.

789 of each individual locus; the primers with the best discriminating power that fit all other design
790 criteria (amplicon size, Tm, distance from cut site) were chosen. All primers are listed in
791 Supplementary File 1.
792 Amplicon PCRs and sequencing sequencing library preparation were performed largely
793 as described above, with the following modifications: 1) PCRs were performed in 384-well
794 format; 2) first-round PCRs were set up using a Biomek FX liquid handling system with a 96-
795 well head (Beckman Coulter); 3) first-round PCR products were diluted into Echo Qualified 384-
796 Well Polypropylene Microplates using the Biomek FX; 4) PCR mastermix for the second-round
797 PCR was dispensed into 384-well PCR plates using the Biomek FX; and 5) diluted first-round
798 PCR products and indexing PCR primers were dispensed into the 384-well PCR plate using an
799 Echo 525 acoustic liquid handler (Labcyte, San Jose, CA). Purification and validation of
800 sequencing libraries, sequencing, classification of sequencing outcomes, and correction for
801 amplicon size were performed as described above. For donor h, a small set of samples did not
802 produce aligning sequencing reads in a first PCR attempt. These samples were repeated manually
803 as described above, after which all but one sample produced aligning sequencing reads. Only
804 successfully prepared samples were included for analysis. For donor i, the sequencing library
805 preparation was repeated independently for >200 loci, which produced near-identical results
806 (Figure 3 – Figure Supplement 4c), validating that the sequencing library preparation strategy is
807 robust and reproducible and that size-dependent amplification efficiency is consistent across
808 PCRs. Samples with >100 size-corrected on-target reads (generally corresponding to >500 raw
809 on-target reads) were included to estimate editing efficiencies. For some pairs of highly
810 homologous loci (e.g. *SFTPA1* and *SFTPA2*), amplicons for both loci were detected with primer
811 pairs designed to amplify each individual locus because it was impossible to design completely

bioRxiv preprint doi: https://doi.org/10.1101/2020.12.22.423985; this version posted December 22, 2020. The copyright holder for this preprint (which was not certified by peer review) is the author/funder, who has granted bioRxiv a license to display the preprint in perpetuity. It is made available under aCC-BY 4.0 International license.

812 specific primer pairs with the criteria used. These amplicons were not excluded when calculating
813 editing efficiency, such that editing efficiency is slightly underestimated for these loci. Results
814 from outcome classification, after correction for size, are listed in Supplementary File 4.
815
816 *Sample sizes and sample size estimation*
817 No sample-size calculation was performed in advance. All results were reproduced in cells from
818 multiple independent donors, following conventions of the field. Within independent
819 experiments, assays were performed in duplicate or triplicate following conventions of the field.
820
821 *Replication and data exclusion*
822 All main findings were derived from experiments with cells from at least 2 independent donors.
823 The main hits from the genetic screen were validated in cells from 2 additional, independent
824 donors. All treatments were performed in duplicate for readout by ELISA and qPCR and in
825 duplicate or triplicate for readout by RNA-seq. Cell counts were generally conducted in
826 duplicate. Information on number of replicates is contained in the figure legends.
827 For identification of differentially expressed genes in RNA-seq, only genes with an
828 average count >2 across all conditions were included for analysis. Exclusion criteria for editing
829 analysis are described in the corresponding methods sections.
830
831 *Data availability*
832 Raw data from RNA-seq of unedited and edited moDCs are available at GEO under accession
833 codes GSE161401 and GSE161466, respectively. Raw data from amplicon sequencing for all
834 samples are available at SRA under accession code PRJNA673198. Processed data from

bioRxiv preprint doi: https://doi.org/10.1101/2020.12.22.423985; this version posted December 22, 2020. The copyright holder for this preprint (which was not certified by peer review) is the author/funder, who has granted bioRxiv a license to display the preprint in perpetuity. It is made available under aCC-BY 4.0 International license.

amplicon sequencing as well as raw and processed data from the genetic screens are provided as supplemental files (Supplementary Files 2, 3, 4).

Code

Amplicon sequencing data were processed using the publicly available pipeline knock-knock (https://github.com/jeffhussmann/knock-knock) (Canaj et al., 2019). RNA-seq data were processed using STAR (Dobin et al., 2013), featureCounts (Liao et al., 2014), and DESeq2 (Love et al., 2014).

bioRxiv preprint doi: https://doi.org/10.1101/2020.12.22.423985; this version posted December 22, 2020. The copyright holder for this preprint (which was not certified by peer review) is the author/funder, who has granted bioRxiv a license to display the preprint in perpetuity. It is made available under aCC-BY 4.0 International license.

Acknowledgements

We thank C. Gross, J. Hiatt, E. Chow (all UCSF), A. May (Chan-Zuckerberg Biohub), J. Kagan (Boston Children's Hospital), J. Chen (UT Southwestern), G. Alberts (Lonza), and all members of the Weissman, Fischbach, and Gross labs for helpful discussions, and E. Chow, D. Martinez, and K. Chaung from the UCSF Center for Advanced Technology for help with sequencing. The Pattern Recognition Receptors and Signaling Pathway arrayed library was provided by Synthego as part of a collaboration agreement. *B. theta* LPS purifications were performed by Biswa P. Choudhury at the UC San Diego GlycoAnalytics Core. JSW is a Howard Hughes Medical Institute Investigator.

Competing Interests

JSW consults for and holds equity in KSQ Therapeutics, Maze Therapeutics, and Tenaya Therapeutics. JSW is a venture partner at 5AM Ventures and a member of the Amgen Scientific Advisory Board. MAF is a co-founder and director of Federation Bio and Viralogic. MJ consults for Maze Therapeutics. JAH consults for Tessera Therapeutics.

bioRxiv preprint doi: https://doi.org/10.1101/2020.12.22.423985; this version posted December 22, 2020. The copyright holder for this preprint (which was not certified by peer review) is the author/funder, who has granted bioRxiv a license to display the preprint in perpetuity. It is made available under aCC-BY 4.0 International license.

References

Antebi, Y.E., Linton, J.M., Klumpe, H., Bintu, B., Gong, M., Su, C., McCardell, R., Elowitz, M.B., 2017. Combinatorial Signal Perception in the BMP Pathway. Cell 170, 1184-1196.e24. https://doi.org/10.1016/j.cell.2017.08.015

Bray, N.L., Pimentel, H., Melsted, P., Pachter, L., 2016. Near-optimal probabilistic RNA-seq quantification. Nature Biotechnology 34, 525–527. https://doi.org/10.1038/nbt.3519

C. Khouili, S., Cook, E.C.L., Hernández-García, E., Martínez-López, M., Conde-Garrosa, R., Iborra, S., 2020. SHP-1 Regulates Antigen Cross-Presentation and Is Exploited by Leishmania to Evade Immunity. Cell Reports 33, 108468. https://doi.org/10.1016/j.celrep.2020.108468

Canaj, H., Hussmann, J.A., Li, H., Beckman, K.A., Goodrich, L., Cho, N.H., Li, Y.J., Santos, D.A., McGeever, A., Stewart, E.M., Pessino, V., Mandegar, M.A., Huang, C., Gan, L., Panning, B., Huang, B., Weissman, J.S., Leonetti, M.D., 2019. Deep profiling reveals substantial heterogeneity of integration outcomes in CRISPR knock-in experiments. bioRxiv 841098. https://doi.org/10.1101/841098

Coats, S.R., Berezow, A.B., To, T.T., Jain, S., Bainbridge, B.W., Banani, K.P., Darveau, R.P., 2011. The Lipid A Phosphate Position Determines Differential Host Toll-Like Receptor 4 Responses to Phylogenetically Related Symbiotic and Pathogenic Bacteria. Infection and Immunity 79, 203–210. https://doi.org/10.1128/IAI.00937-10

Cullen, T.W., Schofield, W.B., Barry, N.A., Putnam, E.E., Rundell, E.A., Trent, M.S., Degnan, P.H., Booth, C.J., Yu, H., Goodman, A.L., 2015. Antimicrobial peptide resistance mediates resilience of prominent gut commensals during inflammation. Science 347, 170–175. https://doi.org/10.1126/science.1260580

bioRxiv preprint doi: https://doi.org/10.1101/2020.12.22.423985; this version posted December 22, 2020. The copyright holder for this preprint (which was not certified by peer review) is the author/funder, who has granted bioRxiv a license to display the preprint in perpetuity. It is made available under aCC-BY 4.0 International license.

d'Hennezel, E., Abubucker, S., Murphy, L.O., Cullen, T.W., 2017. Total Lipopolysaccharide from the Human Gut Microbiome Silences Toll-Like Receptor Signaling. mSystems 2. https://doi.org/10.1128/mSystems.00046-17

Di Lorenzo, F., Pither, M.D., Martufi, M., Scarinci, I., Guzmán-Caldentey, J., Łakomiec, E., Jachymek, W., Bruijns, S.C.M., Santamaría, S.M., Frick, J.-S., van Kooyk, Y., Chiodo, F., Silipo, A., Bernardini, M.L., Molinaro, A., 2020. Pairing Bacteroides vulgatus LPS Structure with Its Immunomodulatory Effects on Human Cellular Models. ACS Cent. Sci. 6, 1602–1616. https://doi.org/10.1021/acscentsci.0c00791

Ding, Y., Guo, Z., Liu, Y., Li, X., Zhang, Q., Xu, X., Gu, Y., Zhang, Y., Zhao, D., Cao, X., 2016. The lectin Siglec-G inhibits dendritic cell cross-presentation by impairing MHC class I–peptide complex formation. Nature Immunology 17, 1167–1175. https://doi.org/10.1038/ni.3535

Dobin, A., Davis, C.A., Schlesinger, F., Drenkow, J., Zaleski, C., Jha, S., Batut, P., Chaisson, M., Gingeras, T.R., 2013. STAR: ultrafast universal RNA-seq aligner. Bioinformatics 29, 15–21. https://doi.org/10.1093/bioinformatics/bts635

Doench, J.G., Fusi, N., Sullender, M., Hegde, M., Vaimberg, E.W., Donovan, K.F., Smith, I., Tothova, Z., Wilen, C., Orchard, R., Virgin, H.W., Listgarten, J., Root, D.E., 2016. Optimized sgRNA design to maximize activity and minimize off-target effects of CRISPR-Cas9. Nature Biotechnology 34, 184–191. https://doi.org/10.1038/nbt.3437

Dunn, J.G., Weissman, J.S., 2016. Plastid: nucleotide-resolution analysis of next-generation sequencing and genomics data. BMC Genomics 17, 958. https://doi.org/10.1186/s12864-016-3278-x

bioRxiv preprint doi: https://doi.org/10.1101/2020.12.22.423985; this version posted December 22, 2020. The copyright holder for this preprint (which was not certified by peer review) is the author/funder, who has granted bioRxiv a license to display the preprint in perpetuity. It is made available under aCC-BY 4.0 International license.

907 Fitzgerald, K.A., Kagan, J.C., 2020. Toll-like Receptors and the Control of Immunity. Cell 180,
908 1044–1066. https://doi.org/10.1016/j.cell.2020.02.041
909 Fitzgerald, K.A., Palsson-McDermott, E.M., Bowie, A.G., Jefferies, C.A., Mansell, A.S., Brady,
910 G., Brint, E., Dunne, A., Gray, P., Harte, M.T., McMurray, D., Smith, D.E., Sims, J.E.,
911 Bird, T.A., O'Neill, L.A.J., 2001. Mal (MyD88-adapter-like) is required for Toll-like
912 receptor-4 signal transduction. Nature 413, 78–83. https://doi.org/10.1038/35092578
913 Fitzgerald, K.A., Rowe, D.C., Barnes, B.J., Caffrey, D.R., Visintin, A., Latz, E., Monks, B.,
914 Pitha, P.M., Golenbock, D.T., 2003. LPS-TLR4 Signaling to IRF-3/7 and NF-κB
915 Involves the Toll Adapters TRAM and TRIF. J Exp Med 198, 1043–1055.
916 https://doi.org/10.1084/jem.20031023
917 Freund, E.C., Lock, J.Y., Oh, J., Maculins, T., Delamarre, L., Bohlen, C.J., Haley, B., Murthy,
918 A., 2020. Efficient gene knockout in primary human and murine myeloid cells by non-
919 viral delivery of CRISPR-Cas9. J Exp Med 217. https://doi.org/10.1084/jem.20191692
920 Garg, A.D., Coulie, P.G., Van den Eynde, B.J., Agostinis, P., 2017. Integrating Next-Generation
921 Dendritic Cell Vaccines into the Current Cancer Immunotherapy Landscape. Trends in
922 Immunology 38, 577–593. https://doi.org/10.1016/j.it.2017.05.006
923 Golenbock, D.T., Hampton, R.Y., Qureshi, N., Takayama, K., Raetz, C.R., 1991. Lipid A-like
924 molecules that antagonize the effects of endotoxins on human monocytes. J. Biol. Chem.
925 266, 19490–19498.
926 Hart, T., Chandrashekhar, M., Aregger, M., Steinhart, Z., Brown, K.R., MacLeod, G., Mis, M.,
927 Zimmermann, M., Fradet-Turcotte, A., Sun, S., Mero, P., Dirks, P., Sidhu, S., Roth, F.P.,
928 Rissland, O.S., Durocher, D., Angers, S., Moffat, J., 2015. High-Resolution CRISPR

bioRxiv preprint doi: https://doi.org/10.1101/2020.12.22.423985; this version posted December 22, 2020. The copyright holder for this preprint (which was not certified by peer review) is the author/funder, who has granted bioRxiv a license to display the preprint in perpetuity. It is made available under aCC-BY 4.0 International license.

929 Screens Reveal Fitness Genes and Genotype-Specific Cancer Liabilities. Cell 163, 1515–
930 1526. https://doi.org/10.1016/j.cell.2015.11.015
931 Hiatt, J., Cavero, D.A., McGregor, M.J., Gordon, D.E., Zheng, W., Budzik, J.M., Roth, T.L.,
932 Haas, K.M., Rathore, U., Meyer-Franke, A., Bouzidi, M.S., Hultquist, J.F.,
933 Wojcechowskyj, J.A., Fontaine, K.A., Pillai, S.K., Cox, J.S., Ernst, J.D., Krogan, N.J.,
934 Marson, A., 2020. Efficient Generation of Isogenic Primary Human Myeloid Cells using
935 CRISPR-Cas9 Ribonucleoproteins. bioRxiv 2020.03.13.991414.
936 https://doi.org/10.1101/2020.03.13.991414
937 Jacobson, A.N., Choudhury, B.P., Fischbach, M.A., 2018. The Biosynthesis of
938 Lipooligosaccharide from *Bacteroides thetaiotaomicron*. mBio 9.
939 https://doi.org/10.1128/mBio.02289-17
940 Kaelin, W.G., 2012. Use and Abuse of RNAi to Study Mammalian Gene Function. Science 337,
941 421–422. https://doi.org/10.1126/science.1225787
942 Laustsen, A., Bak, R.O., Krapp, C., Kjær, L., Egedahl, J.H., Petersen, C.C., Pillai, S., Tang,
943 H.Q., Uldbjerg, N., Porteus, M., Roan, N.R., Nyegaard, M., Denton, P.W., Jakobsen,
944 M.R., 2018. Interferon priming is essential for human CD34+ cell-derived plasmacytoid
945 dendritic cell maturation and function. Nature Communications 9, 3525.
946 https://doi.org/10.1038/s41467-018-05816-y
947 Leenay, R.T., Aghazadeh, A., Hiatt, J., Tse, D., Roth, T.L., Apathy, R., Shifrut, E., Hultquist,
948 J.F., Krogan, N., Wu, Z., Cirolia, G., Canaj, H., Leonetti, M.D., Marson, A., May, A.P.,
949 Zou, J., 2019. Large dataset enables prediction of repair after CRISPR–Cas9 editing in
950 primary T cells. Nature Biotechnology 37, 1034–1037. https://doi.org/10.1038/s41587-
951 019-0203-2

bioRxiv preprint doi: https://doi.org/10.1101/2020.12.22.423985; this version posted December 22, 2020. The copyright holder for this preprint (which was not certified by peer review) is the author/funder, who has granted bioRxiv a license to display the preprint in perpetuity. It is made available under aCC-BY 4.0 International license.

952 Liao, Y., Smyth, G.K., Shi, W., 2014. featureCounts: an efficient general purpose program for
953 assigning sequence reads to genomic features. Bioinformatics 30, 923–930.
954 https://doi.org/10.1093/bioinformatics/btt656
955 Love, M.I., Huber, W., Anders, S., 2014. Moderated estimation of fold change and dispersion for
956 RNA-seq data with DESeq2. Genome Biology 15, 550. https://doi.org/10.1186/s13059-
957 014-0550-8
958 Lucas, C., Wong, P., Klein, J., Castro, T.B.R., Silva, J., Sundaram, M., Ellingson, M.K., Mao, T.,
959 Oh, J.E., Israelow, B., Takahashi, T., Tokuyama, M., Lu, P., Venkataraman, A., Park, A.,
960 Mohanty, S., Wang, H., Wyllie, A.L., Vogels, C.B.F., Earnest, R., Lapidus, S., Ott, I.M.,
961 Moore, A.J., Muenker, M.C., Fournier, J.B., Campbell, M., Odio, C.D., Casanovas-
962 Massana, A., Herbst, R., Shaw, A.C., Medzhitov, R., Schulz, W.L., Grubaugh, N.D.,
963 Cruz, C.D., Farhadian, S., Ko, A.I., Omer, S.B., Iwasaki, A., 2020. Longitudinal analyses
964 reveal immunological misfiring in severe COVID-19. Nature 584, 463–469.
965 https://doi.org/10.1038/s41586-020-2588-y
966 Mali, P., Yang, L., Esvelt, K.M., Aach, J., Guell, M., DiCarlo, J.E., Norville, J.E., Church, G.M.,
967 2013. RNA-Guided Human Genome Engineering via Cas9. Science 339, 823–826.
968 https://doi.org/10.1126/science.1232033
969 Merad, M., Sathe, P., Helft, J., Miller, J., Mortha, A., 2013. The Dendritic Cell Lineage:
970 Ontogeny and Function of Dendritic Cells and Their Subsets in the Steady State and the
971 Inflamed Setting. Annu. Rev. Immunol. 31, 563–604. https://doi.org/10.1146/annurev-
972 immunol-020711-074950
973 Pereira, N.L., Ahmad, F., Cummins, N.W., Byku, M., Morris, A.A., Owens, A., Tuteja, S.,
974 Cresci, S., 2020. COVID-19: Understanding Inter-Individual Variability and Implications

bioRxiv preprint doi: https://doi.org/10.1101/2020.12.22.423985; this version posted December 22, 2020. The copyright holder for this preprint (which was not certified by peer review) is the author/funder, who has granted bioRxiv a license to display the preprint in perpetuity. It is made available under aCC-BY 4.0 International license.

975 for Precision Medicine. Mayo Clinic Proceedings.
976 https://doi.org/10.1016/j.mayocp.2020.11.024
977 Poltorak, A., He, X., Smirnova, I., Liu, M.-Y., Huffel, C.V., Du, X., Birdwell, D., Alejos, E.,
978 Silva, M., Galanos, C., Freudenberg, M., Ricciardi-Castagnoli, P., Layton, B., Beutler,
979 B., 1998. Defective LPS Signaling in C3H/HeJ and C57BL/10ScCr Mice: Mutations in
980 Tlr4 Gene. Science 282, 2085–2088. https://doi.org/10.1126/science.282.5396.2085
981 Porter, N.T., Canales, P., Peterson, D.A., Martens, E.C., 2017. A Subset of Polysaccharide
982 Capsules in the Human Symbiont Bacteroides thetaiotaomicron Promote Increased
983 Competitive Fitness in the Mouse Gut. Cell Host & Microbe 22, 494-506.e8.
984 https://doi.org/10.1016/j.chom.2017.08.020
985 Pulendran, B., Davis, M.M., 2020. The science and medicine of human immunology. Science
986 369. https://doi.org/10.1126/science.aay4014
987 Riggan, L., Hildreth, A.D., Rolot, M., Wong, Y.-Y., Satyadi, W., Sun, R., Huerta, C.,
988 O'Sullivan, T.E., 2020. CRISPR-Cas9 Ribonucleoprotein-Mediated Genomic Editing in
989 Mature Primary Innate Immune Cells. Cell Reports 31, 107651.
990 https://doi.org/10.1016/j.celrep.2020.107651
991 Roth, T.L., Puig-Saus, C., Yu, R., Shifrut, E., Carnevale, J., Li, P.J., Hiatt, J., Saco, J.,
992 Krystofinski, P., Li, H., Tobin, V., Nguyen, D.N., Lee, M.R., Putnam, A.L., Ferris, A.L.,
993 Chen, J.W., Schickel, J.-N., Pellerin, L., Carmody, D., Alkorta-Aranburu, G., del Gaudio,
994 D., Matsumoto, H., Morell, M., Mao, Y., Cho, M., Quadros, R.M., Gurumurthy, C.B.,
995 Smith, B., Haugwitz, M., Hughes, S.H., Weissman, J.S., Schumann, K., Esensten, J.H.,
996 May, A.P., Ashworth, A., Kupfer, G.M., Greeley, S.A.W., Bacchetta, R., Meffre, E.,
997 Roncarolo, M.G., Romberg, N., Herold, K.C., Ribas, A., Leonetti, M.D., Marson, A.,

bioRxiv preprint doi: https://doi.org/10.1101/2020.12.22.423985; this version posted December 22, 2020. The copyright holder for this preprint (which was not certified by peer review) is the author/funder, who has granted bioRxiv a license to display the preprint in perpetuity. It is made available under aCC-BY 4.0 International license.

2018. Reprogramming human T cell function and specificity with non-viral genome targeting. Nature 559, 405–409. https://doi.org/10.1038/s41586-018-0326-5

Sallusto, F., Lanzavecchia, A., 1994. Efficient presentation of soluble antigen by cultured human dendritic cells is maintained by granulocyte/macrophage colony-stimulating factor plus interleukin 4 and downregulated by tumor necrosis factor alpha. J Exp Med 179, 1109–1118. https://doi.org/10.1084/jem.179.4.1109

Sanz, J., Randolph, H.E., Barreiro, L.B., 2018. Genetic and evolutionary determinants of human population variation in immune responses. Current Opinion in Genetics & Development, Genetics of Human Origins 53, 28–35. https://doi.org/10.1016/j.gde.2018.06.009

Schumann, K., Lin, S., Boyer, E., Simeonov, D.R., Subramaniam, M., Gate, R.E., Haliburton, G.E., Ye, C.J., Bluestone, J.A., Doudna, J.A., Marson, A., 2015. Generation of knock-in primary human T cells using Cas9 ribonucleoproteins. PNAS 112, 10437–10442. https://doi.org/10.1073/pnas.1512503112

Song, X.-T., 2014. Genetic Modification of Dendritic Cells with RNAi, in: Lawman, M.J.P., Lawman, P.D. (Eds.), Cancer Vaccines: Methods and Protocols, Methods in Molecular Biology. Springer, New York, NY, pp. 119–130. https://doi.org/10.1007/978-1-4939-0345-0_11

Stefan, K.L., Kim, M.V., Iwasaki, A., Kasper, D.L., 2020. Commensal Microbiota Modulation of Natural Resistance to Virus Infection. Cell 0. https://doi.org/10.1016/j.cell.2020.10.047

Steimle, A., Michaelis, L., Di Lorenzo, F., Kliem, T., Münzner, T., Maerz, J.K., Schäfer, A., Lange, A., Parusel, R., Gronbach, K., Fuchs, K., Silipo, A., Öz, H.H., Pichler, B.J., Autenrieth, I.B., Molinaro, A., Frick, J.-S., 2019. Weak Agonistic LPS Restores Intestinal

bioRxiv preprint doi: https://doi.org/10.1101/2020.12.22.423985; this version posted December 22, 2020. The copyright holder for this preprint (which was not certified by peer review) is the author/funder, who has granted bioRxiv a license to display the preprint in perpetuity. It is made available under aCC-BY 4.0 International license.

1020 Immune Homeostasis. Molecular Therapy 27, 1974–1991.
1021 https://doi.org/10.1016/j.ymthe.2019.07.007
1022 Stoner, R., Maures, T., Conant, D., 2019. METHODS AND SYSTEMS FOR GUIDE RNA
1023 DESIGN AND USE. U.S. Patent 2019/0382797 A1.
1024 Sun, T., Nguyen, A., Gommerman, J.L., 2020. Dendritic Cell Subsets in Intestinal Immunity and
1025 Inflammation. The Journal of Immunology 204, 1075–1083.
1026 https://doi.org/10.4049/jimmunol.1900710
1027 Tan, Y., Zanoni, I., Cullen, T.W., Goodman, A.L., Kagan, J.C., 2015. Mechanisms of Toll-like
1028 Receptor 4 Endocytosis Reveal a Common Immune-Evasion Strategy Used by
1029 Pathogenic and Commensal Bacteria. Immunity 43, 909–922.
1030 https://doi.org/10.1016/j.immuni.2015.10.008
1031 Tsherniak, A., Vazquez, F., Montgomery, P.G., Weir, B.A., Kryukov, G., Cowley, G.S., Gill, S.,
1032 Harrington, W.F., Pantel, S., Krill-Burger, J.M., Meyers, R.M., Ali, L., Goodale, A., Lee,
1033 Y., Jiang, G., Hsiao, J., Gerath, W.F.J., Howell, S., Merkel, E., Ghandi, M., Garraway,
1034 L.A., Root, D.E., Golub, T.R., Boehm, J.S., Hahn, W.C., 2017. Defining a Cancer
1035 Dependency Map. Cell 170, 564-576.e16. https://doi.org/10.1016/j.cell.2017.06.010
1036 Vatanen, T., Kostic, A.D., d'Hennezel, E., Siljander, H., Franzosa, E.A., Yassour, M., Kolde, R.,
1037 Vlamakis, H., Arthur, T.D., Hämäläinen, A.-M., Peet, A., Tillmann, V., Uibo, R.,
1038 Mokurov, S., Dorshakova, N., Ilonen, J., Virtanen, S.M., Szabo, S.J., Porter, J.A.,
1039 Lähdesmäki, H., Huttenhower, C., Gevers, D., Cullen, T.W., Knip, M., Xavier, R.J.,
1040 2016. Variation in Microbiome LPS Immunogenicity Contributes to Autoimmunity in
1041 Humans. Cell 165, 842–853. https://doi.org/10.1016/j.cell.2016.04.007

bioRxiv preprint doi: https://doi.org/10.1101/2020.12.22.423985; this version posted December 22, 2020. The copyright holder for this preprint (which was not certified by peer review) is the author/funder, who has granted bioRxiv a license to display the preprint in perpetuity. It is made available under aCC-BY 4.0 International license.

1042 Wculek, S.K., Cueto, F.J., Mujal, A.M., Melero, I., Krummel, M.F., Sancho, D., 2020. Dendritic
1043 cells in cancer immunology and immunotherapy. Nature Reviews Immunology 20, 7–24.
1044 https://doi.org/10.1038/s41577-019-0210-z
1045 Weintraub, A., Zähringer, U., Wollenweber, H.-W., Seydel, U., Rietschel, E.T., 1989. Structural
1046 characterization of the lipid A component of Bacteroides fragilis strain NCTC 9343
1047 lipopolysaccharide. European Journal of Biochemistry 183, 425–431.
1048 https://doi.org/10.1111/j.1432-1033.1989.tb14945.x
1049 Werts, C., Tapping, R.I., Mathison, J.C., Chuang, T.-H., Kravchenko, V., Saint Girons, I.,
1050 Haake, D.A., Godowski, P.J., Hayashi, F., Ozinsky, A., Underhill, D.M., Kirschning,
1051 C.J., Wagner, H., Aderem, A., Tobias, P.S., Ulevitch, R.J., 2001. Leptospiral
1052 lipopolysaccharide activates cells through a TLR2-dependent mechanism. Nature
1053 Immunology 2, 346–352. https://doi.org/10.1038/86354
1054 Wexler, A.G., Goodman, A.L., 2017. An insider's perspective: Bacteroides as a window into the
1055 microbiome. Nature Microbiology 2, 1–11. https://doi.org/10.1038/nmicrobiol.2017.26
1056 Yamamoto, M., Sato, S., Hemmi, H., Hoshino, K., Kaisho, T., Sanjo, H., Takeuchi, O.,
1057 Sugiyama, M., Okabe, M., Takeda, K., Akira, S., 2003. Role of Adaptor TRIF in the
1058 MyD88-Independent Toll-Like Receptor Signaling Pathway. Science 301, 640–643.
1059 https://doi.org/10.1126/science.1087262
1060 Yamamoto, M., Sato, S., Mori, K., Hoshino, K., Takeuchi, O., Takeda, K., Akira, S., 2002.
1061 Cutting Edge: A Novel Toll/IL-1 Receptor Domain-Containing Adapter That
1062 Preferentially Activates the IFN-β Promoter in the Toll-Like Receptor Signaling. The
1063 Journal of Immunology 169, 6668–6672. https://doi.org/10.4049/jimmunol.169.12.6668

bioRxiv preprint doi: https://doi.org/10.1101/2020.12.22.423985; this version posted December 22, 2020. The copyright holder for this preprint (which was not certified by peer review) is the author/funder, who has granted bioRxiv a license to display the preprint in perpetuity. It is made available under aCC-BY 4.0 International license.

1064 Ye, J., Coulouris, G., Zaretskaya, I., Cutcutache, I., Rozen, S., Madden, T.L., 2012. Primer-
1065 BLAST: A tool to design target-specific primers for polymerase chain reaction. BMC
1066 Bioinformatics 13, 134. https://doi.org/10.1186/1471-2105-13-134
1067 Zanoni, I., Ostuni, R., Marek, L.R., Barresi, S., Barbalat, R., Barton, G.M., Granucci, F., Kagan,
1068 J.C., 2011. CD14 Controls the LPS-Induced Endocytosis of Toll-like Receptor 4. Cell
1069 147, 868–880. https://doi.org/10.1016/j.cell.2011.09.051
1070 Zhu, T., Liang, C., Meng, Z., Li, Y., Wu, Y., Guo, S., Zhang, R., 2017. PrimerServer: a high-
1071 throughput primer design and specificity-checking platform. bioRxiv 181941.
1072 https://doi.org/10.1101/181941
1073
1074

bioRxiv preprint doi: https://doi.org/10.1101/2020.12.22.423985; this version posted December 22, 2020. The copyright holder for this preprint (which was not certified by peer review) is the author/funder, who has granted bioRxiv a license to display the preprint in perpetuity. It is made available under aCC-BY 4.0 International license.

1075 **Figures and Figure Legends**

Figure 1

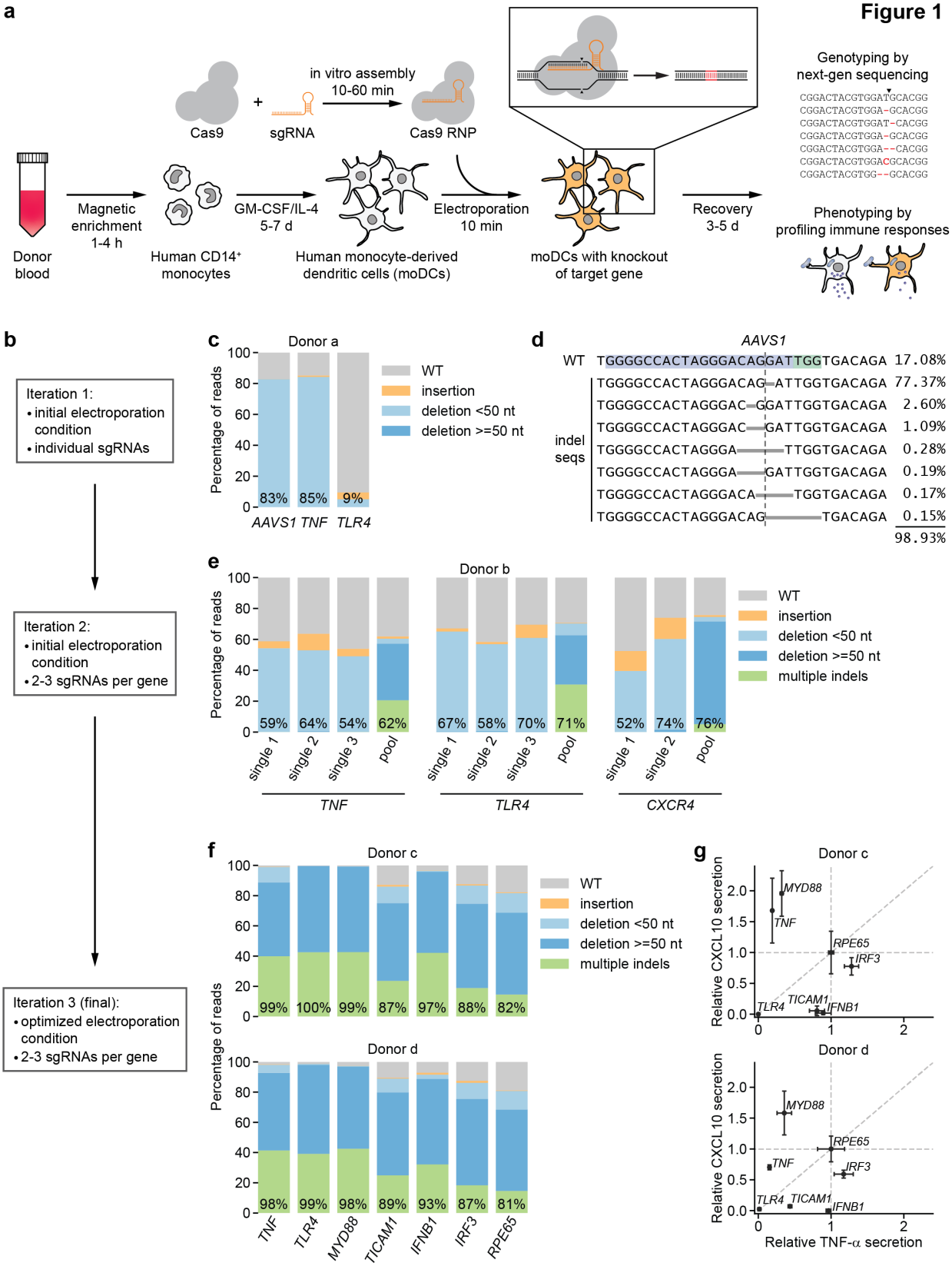

1076

bioRxiv preprint doi: https://doi.org/10.1101/2020.12.22.423985; this version posted December 22, 2020. The copyright holder for this preprint (which was not certified by peer review) is the author/funder, who has granted bioRxiv a license to display the preprint in perpetuity. It is made available under aCC-BY 4.0 International license.

Figure 1. CRISPR/Cas9-based strategy for gene knockout in human moDCs. **(a)** Schematic outline of the strategy. **(b)** Flow chart delineating optimization. **(c)** Percentage of genomic DNA reads assigned to different classes of outcomes after targeting each locus with Cas9 RNPs in condition P1, CB-150. Labeled values indicate total percentage of reads with a non-WT sequence. **(d)** Individual editing outcomes at the *AAVS1* locus accounting for at least 0.15% of on-target reads. Horizontal gray bars denote deletions. Vertical dashed line denotes Cas9 cut site. **(e)** Outcome classification, as in **(c)**, after targeting indicated loci with single or multi-sgRNA Cas9 RNPs. **(f)** Outcome classification, as in **(c)**, after targeting 7 loci with multi-sgRNA Cas9 RNPs in moDCs from two independent donors. **(g)** Production of TNF-α and CXCL10 by knockout moDCs challenged with 100 ng/mL *E. coli* O55 LPS, normalized to cell numbers and to cytokine production in moDCs with knockout of *RPE65*. Data represent mean and standard deviation of 2 independent treatments for both TNF-α and CXCL10 levels.
See also Figure 1 – Figure Supplement 1, Figure 1 – Figure Supplement 2, and Figure 1 – Figure Supplement 3.

bioRxiv preprint doi: https://doi.org/10.1101/2020.12.22.423985; this version posted December 22, 2020. The copyright holder for this preprint (which was not certified by peer review) is the author/funder, who has granted bioRxiv a license to display the preprint in perpetuity. It is made available under aCC-BY 4.0 International license.

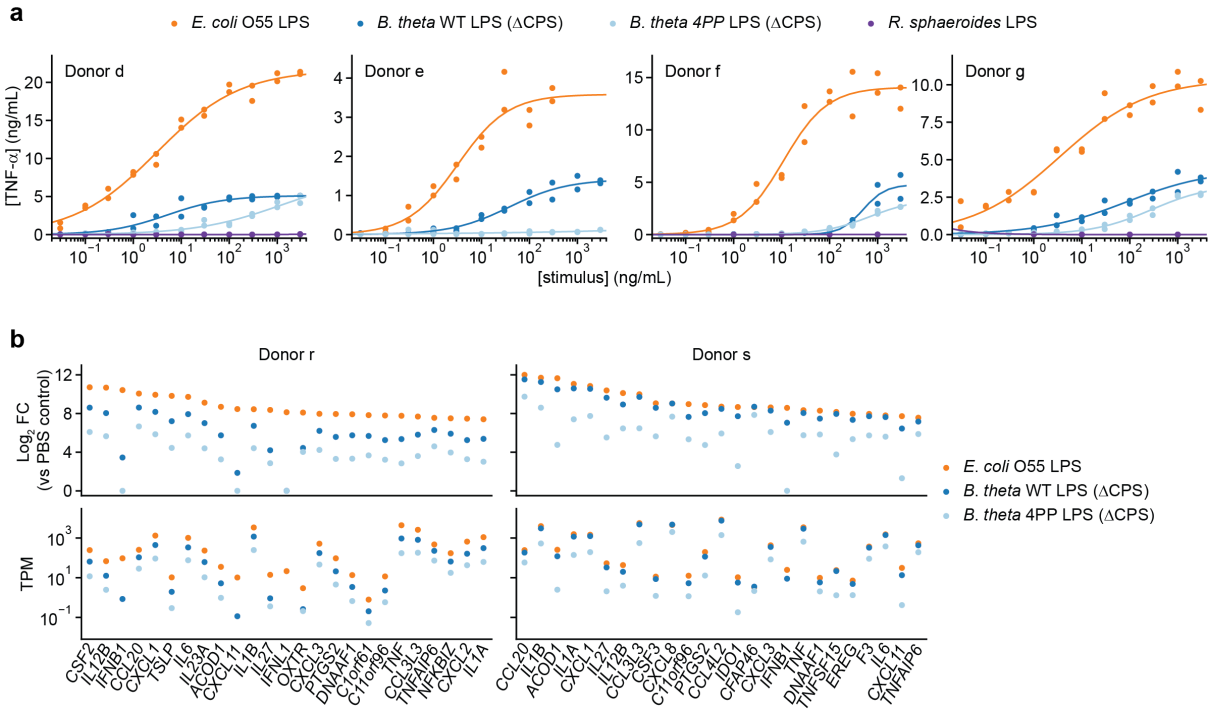

Figure 2. Responses of human moDCs to LPSs are specific to bacterial species and human donor. **(a)** TNF-α secretion after stimulation of moDCs from 4 independent donors with titration series of the indicated LPSs. Cells from donor e were not treated with *R. sphaeroides* LPS. Each data point represents an independent treatment of 20,000 moDCs. Lines denote a Hill curve fit. **(b)** Expression levels of selected genes after stimulation of moDCs from two donors with 10 ng/mL *E. coli* O55 LPS, 100 ng/mL *B. theta* WT LPS, or 100 ng/mL *B. theta* 4PP LPS, as determined by RNA-seq. Log_2 fold-changes compared to PBS-treated control cells or transcript counts per million are shown for the 25 genes with the largest log_2 fold-changes after treatment with *E. coli* O55 LPS. *B. theta* WT LPS elicits weaker upregulation of genes than *E. coli* O55 LPS, with a more pronounced difference for genes downstream of TRIF such as *IFNB1*. *B. theta* 4PP LPS elicits even weaker upregulation of genes. Data represent means obtained from three independent treatment replicates for each treatment and donor.

See also Figure 2 – Figure Supplement 1 and Figure 2 – Figure Supplement 2.

bioRxiv preprint doi: https://doi.org/10.1101/2020.12.22.423985; this version posted December 22, 2020. The copyright holder for this preprint (which was not certified by peer review) is the author/funder, who has granted bioRxiv a license to display the preprint in perpetuity. It is made available under aCC-BY 4.0 International license.

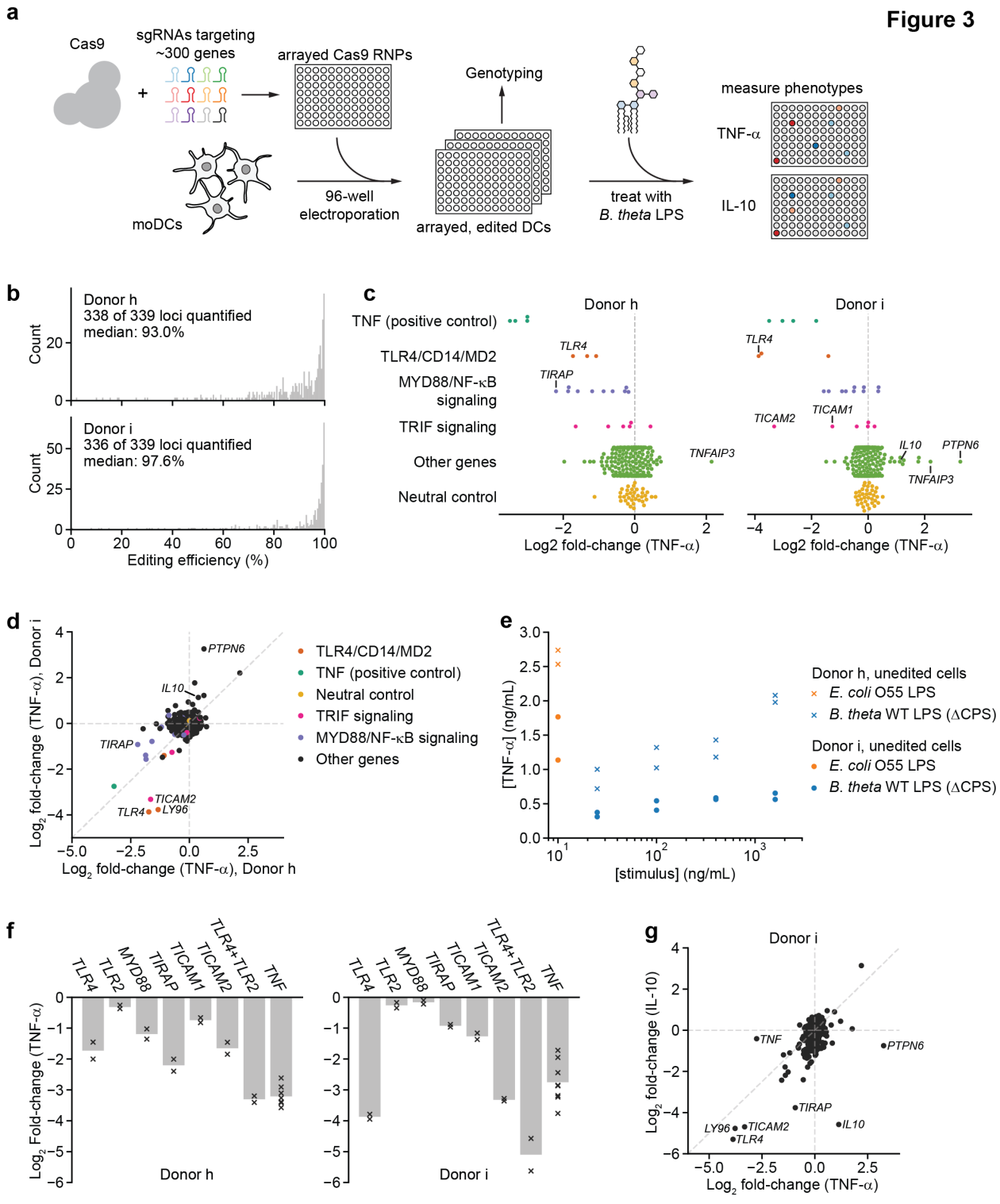

Figure 3. An arrayed genetic screen reveals how moDCs recognize LPS from a human gut bacterium and mechanisms of inter-individual variation. **(a)** Schematic of genetic screen. **(b)**

bioRxiv preprint doi: https://doi.org/10.1101/2020.12.22.423985; this version posted December 22, 2020. The copyright holder for this preprint (which was not certified by peer review) is the author/funder, who has granted bioRxiv a license to display the preprint in perpetuity. It is made available under aCC-BY 4.0 International license.

Observed editing efficiencies for loci targeted in the screen. Efficiencies were not obtained for 1 locus for donor h and 3 loci for donor i due to PCR failures; no locus failed for both donors. **(c)** TNF-α secretion of knockout moDC populations from two independent donors, displayed as $\log_2$ fold-changes compared to neutral controls within each of the four 96-well plates and normalized to cell counts. Each data point represents the mean of two treatment replicates and two cell count replicates. **(d)** Comparison of TNF-α secretion from **(c)** for the two donors. **(e)** TNF-α secretion after stimulation of unedited moDCs (from no pulse/no RNP wells) from both donors with different concentrations of the indicated LPSs. Each data point represents an independent treatment. **(f)** TNF-α secretion for selected moDC knockout populations including moDCs with simultaneous knockout of *TLR4* and *TLR2*. Data are shown as individual measurements (×) and mean of all treatment replicates (bars). **(g)** Comparison of TNF-α and IL-10 secretion from knockout moDC populations for moDCs derived from donor i. Each data point represents the mean of two treatment replicates and two cell count replicates for TNF-α secretion and data from a single treatment replicate and two cell count replicates for IL-10 secretion.

See also Figure 3 – Figure Supplement 1, Figure 3 – Figure Supplement 2, Figure 3 – Figure Supplement 3, Figure 3 – Figure Supplement 4, Figure 3 – Figure Supplement 5, and Figure 3 – Figure Supplement 6.

bioRxiv preprint doi: https://doi.org/10.1101/2020.12.22.423985; this version posted December 22, 2020. The copyright holder for this preprint (which was not certified by peer review) is the author/funder, who has granted bioRxiv a license to display the preprint in perpetuity. It is made available under aCC-BY 4.0 International license.

Figure Supplements and Figure Supplement Legends

Figure 1 - Figure Supplement 1

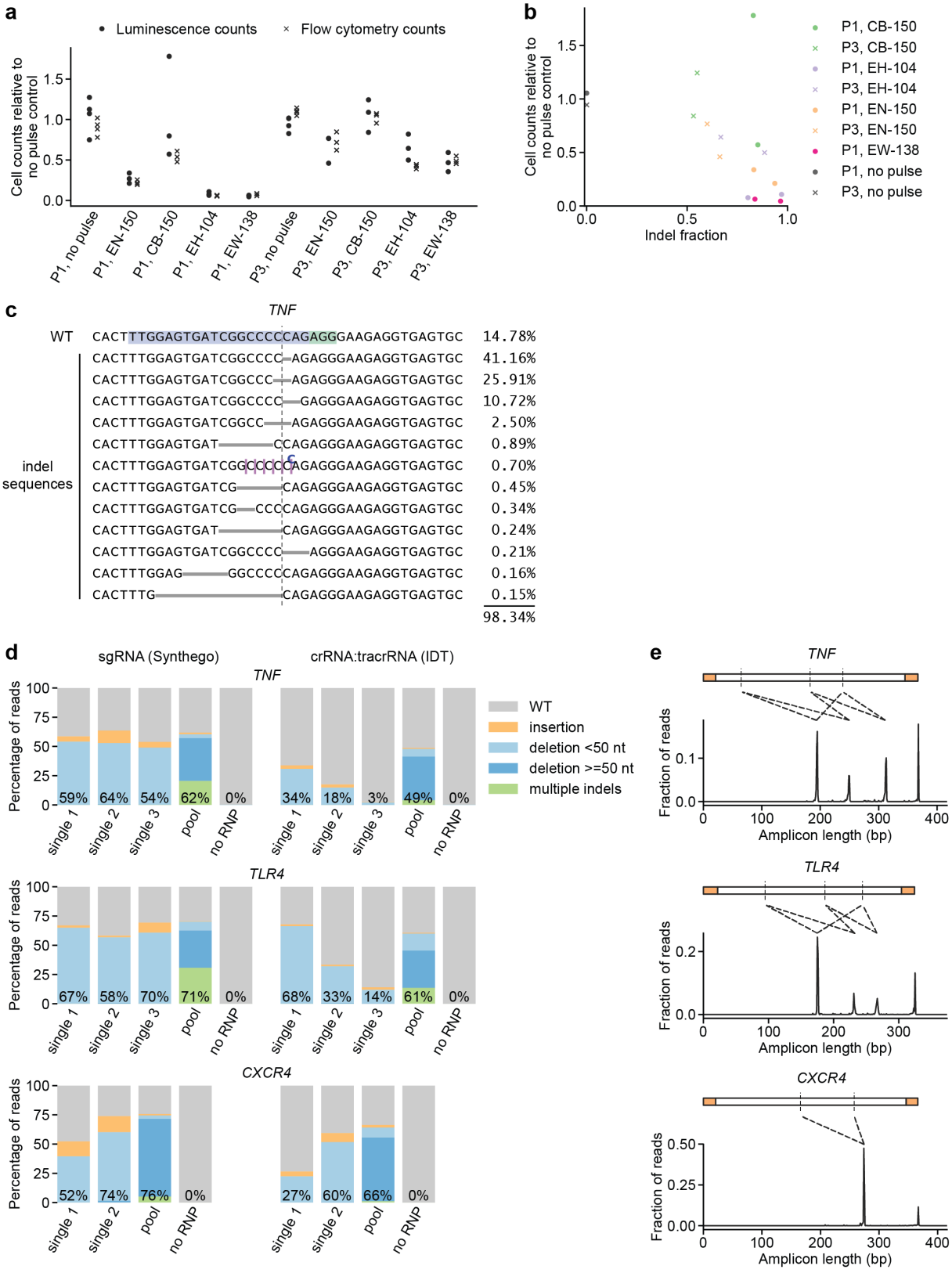

bioRxiv preprint doi: https://doi.org/10.1101/2020.12.22.423985; this version posted December 22, 2020. The copyright holder for this preprint (which was not certified by peer review) is the author/funder, who has granted bioRxiv a license to display the preprint in perpetuity. It is made available under aCC-BY 4.0 International license.

Figure 1 – Figure Supplement 1. Additional characterization of initial conditions for moDC genome editing strategy. **(a)** Cell counts relative to no pulse control cells determined by two methods 3 d (flow cytometry) or 5 d (luminescence) after electroporation of moDCs in indicated conditions. **(b)** Comparison of indel fraction and cell counts measured in different electroporation conditions, identifying condition P1, CB-150 as a condition with low toxicity and high editing efficiency. **(c)** Individual editing outcomes at the *TNF* locus accounting for at least 0.15% of on-target reads after editing in condition P1, CB-150. Horizontal gray bars denote deletions. Vertical dashed line denotes Cas9 cut site. Superscripted bases denote insertions. Due to the presence of a C homopolymer at the cut site, the location of some short deletions and insertions cannot be unambiguously inferred; the most likely location is denoted. **(d)** Percentage of genomic DNA reads assigned to different classes of outcomes after targeting each locus with single or multi-sgRNA Cas9 RNPs in condition P1, CB-150. Cas9 RNPs were formed either with sgRNAs (left) or crRNA:tracrRNA complexes (right). Labeled values indicate total percentage of reads with a non-WT sequence. **(e)** Distribution of amplicon lengths for moDCs electroporated with multi-sgRNA Cas9 RNPs (in the sgRNA format). Observed amplicons correspond to deletions of regions between sgRNA cut sites, as indicated by the diagrams. Amplicons are depicted with the primer binding sequences in orange and sgRNA cut sites as vertical dashed lines.

bioRxiv preprint doi: https://doi.org/10.1101/2020.12.22.423985; this version posted December 22, 2020. The copyright holder for this preprint (which was not certified by peer review) is the author/funder, who has granted bioRxiv a license to display the preprint in perpetuity. It is made available under aCC-BY 4.0 International license.

Figure 1 - Figure Supplement 2

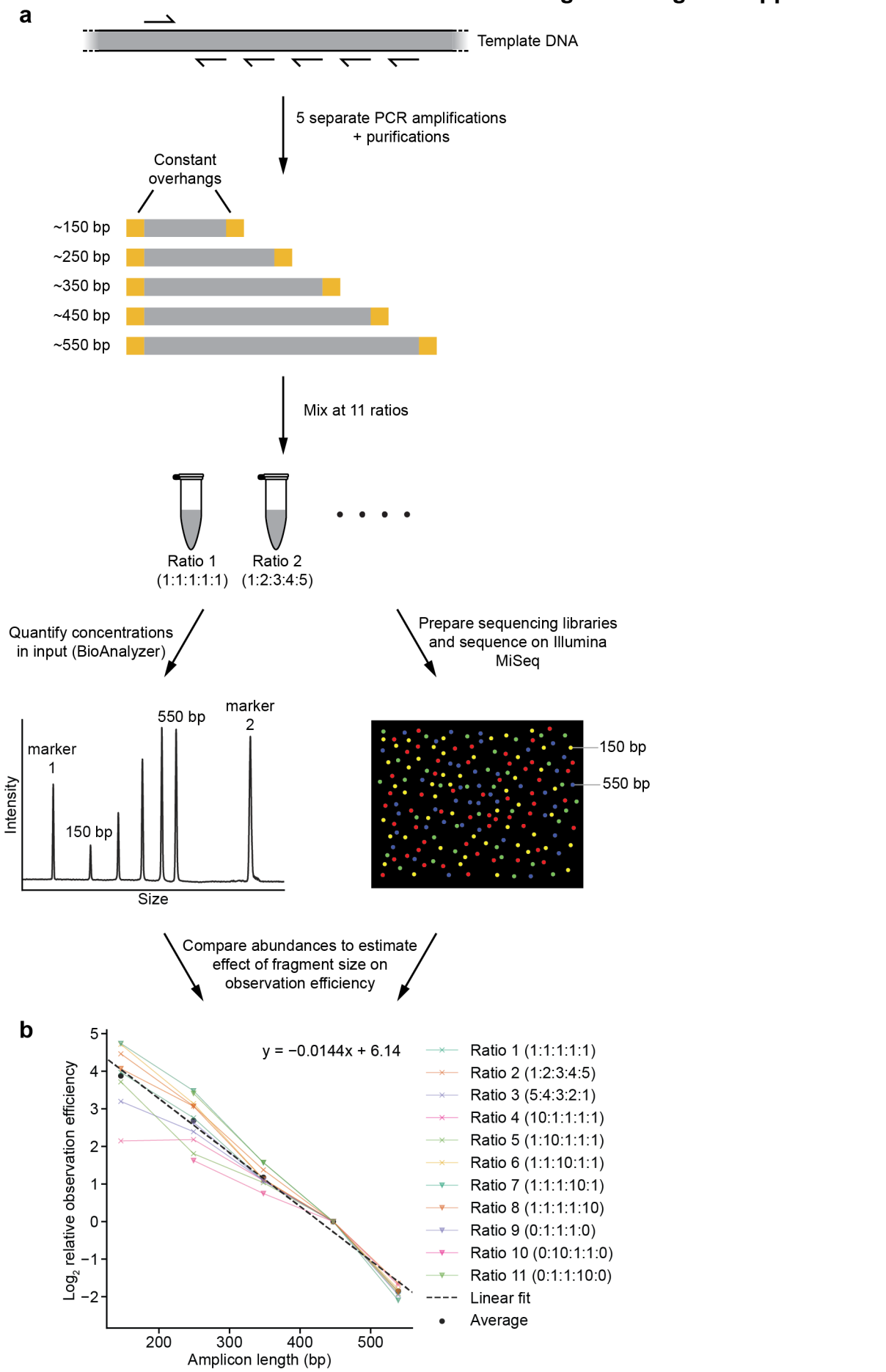

bioRxiv preprint doi: https://doi.org/10.1101/2020.12.22.423985; this version posted December 22, 2020. The copyright holder for this preprint (which was not certified by peer review) is the author/funder, who has granted bioRxiv a license to display the preprint in perpetuity. It is made available under aCC-BY 4.0 International license.

Figure 1 – Figure Supplement 2. Strategy to measure effect of amplicon size on observation (amplification + sequencing) efficiency. **(a)** Schematic outline of strategy. See methods for details. **(b)** Comparison of calculated observation efficiencies and fragment size for each fragment with each of the 11 reaction ratios. Dotted line represents fit derived from a linear regression, with coefficients indicated.

bioRxiv preprint doi: https://doi.org/10.1101/2020.12.22.423985; this version posted December 22, 2020. The copyright holder for this preprint (which was not certified by peer review) is the author/funder, who has granted bioRxiv a license to display the preprint in perpetuity. It is made available under aCC-BY 4.0 International license.

Figure 1 - Figure Supplement 3

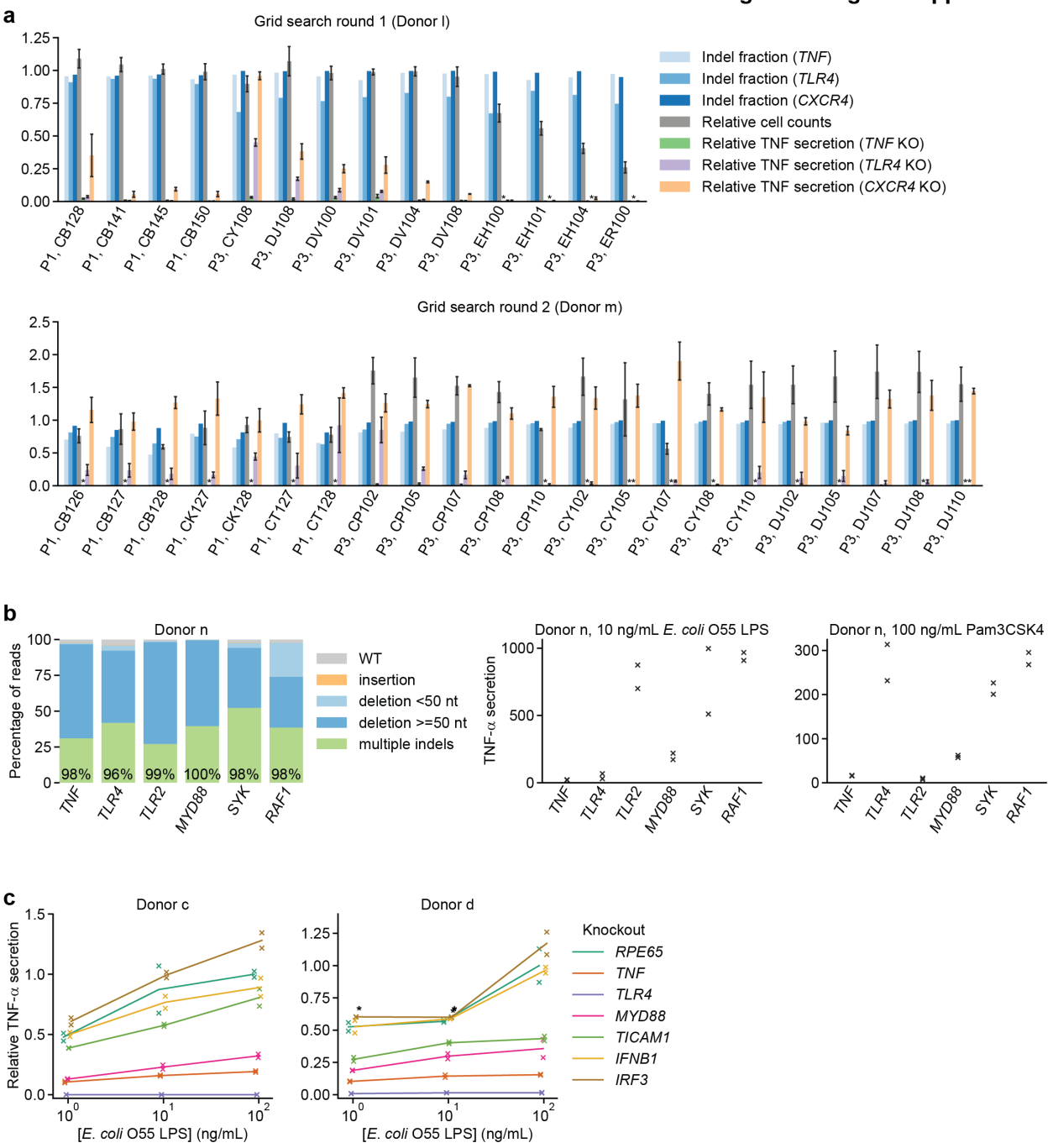

Figure 1 – Figure Supplement 3. Identification of an optimal electroporation condition for moDC genome editing. **(a)** Results from two successive grid searches of electroporation conditions. Ideal conditions have high indel fraction at all loci, high cell counts, low TNF-α secretion in response to 10 ng/mL *E. coli* LPS with knockout of *TNF* and *TLR4*, and high TNF-α

bioRxiv preprint doi: https://doi.org/10.1101/2020.12.22.423985; this version posted December 22, 2020. The copyright holder for this preprint (which was not certified by peer review) is the author/funder, who has granted bioRxiv a license to display the preprint in perpetuity. It is made available under aCC-BY 4.0 International license.

secretion with knockout of *CXCR4*. TNF-α secretion was normalized to cell counts. Indel fractions represent data from a single measurement. Cell counts represent mean count ± standard deviation from two independent wells. TNF-α secretion values represent mean ± standard deviation of two independent treatments, normalized to cell counts. (*) indicates signal below detection limit. **(b)** Left: Percentage of genomic DNA reads assigned to different classes of outcomes after targeting each locus with multi-sgRNA Cas9 RNPs. Labeled values indicate total percentage of reads with a non-WT sequence. Right: Production of TNF-α by knockout moDCs challenged with 10 ng/mL *E. coli* O55 LPS or 100 ng/mL Pam3CSK4, normalized to cell counts. Data represent two independent treatments, normalized to cell count obtained from replicate measurements. **(c)** Production of TNF-α by knockout moDCs challenged with indicated concentrations of *E. coli* O55 LPS, normalized to cell counts and to TNF-α production by moDCs with knockout of *RPE65* and treated with the highest concentration of *E. coli* O55 LPS. All samples were treated with identical LPS concentrations, but x-values are slightly offset by sample for clarity. Data represent two independent treatments, normalized to cell count obtained from replicate measurements. (*) indicates sample saturated during measurement of TNF-α secretion. Data from treatment with 100 ng/mL *E. coli* O55 LPS are also plotted in Figure 1g.

bioRxiv preprint doi: https://doi.org/10.1101/2020.12.22.423985; this version posted December 22, 2020. The copyright holder for this preprint (which was not certified by peer review) is the author/funder, who has granted bioRxiv a license to display the preprint in perpetuity. It is made available under aCC-BY 4.0 International license.

Figure 2 - Figure Supplement 1

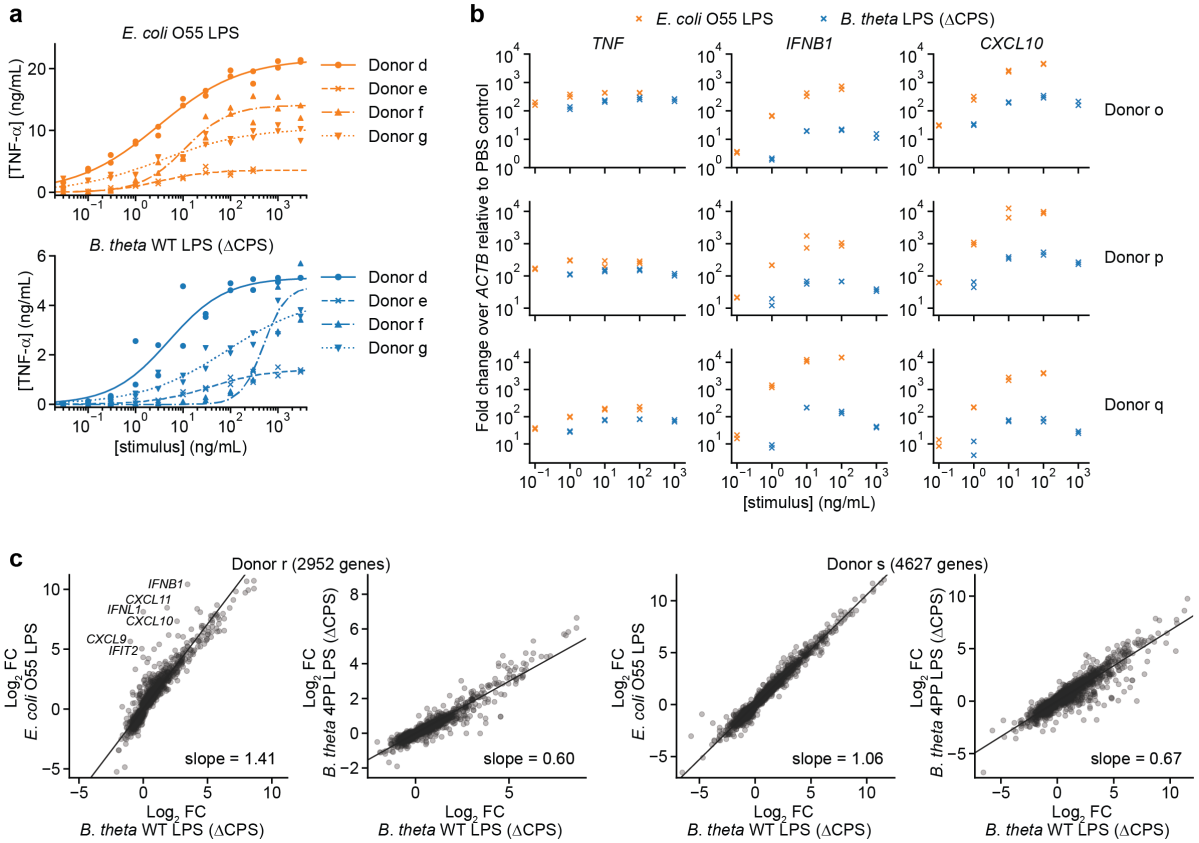

Figure 2 – Figure Supplement 1. *B. theta* LPS and *E. coli* LPS elicit different responses from moDCs with responses that vary by donor. **(a)** Responses to individual LPSs from Figure 2a plotted by donor to highlight differences in response magnitude and EC_{50}. **(b)** Fold-changes in gene expression for *TNF* (activated by MYD88 and TRIF), *IFNB1*, and *CXCL10* (both activated only by TRIF) upon treatment with *B. theta* LPS or *E. coli* LPS for moDCs derived from three independent donors, measured by qPCR as $2^{-\Delta\Delta Cp}$, calculated as the difference in C_p of the target gene compared to *ACTB* (ΔCp) and normalized to the same quantity for PBS-treated cells (ΔΔCp). Data represent two independent treatments and RNA extractions. Each data point represents the mean of three technical replicates. **(c)** Comparison of $\log_2$ fold-changes from RNA-seq data for all genes differentially expressed with $p < 0.01$ with any treatment, as determined by DeSeq2 (Love et al., 2014). *B. theta* WT LPS elicits weaker upregulation of genes

bioRxiv preprint doi: https://doi.org/10.1101/2020.12.22.423985; this version posted December 22, 2020. The copyright holder for this preprint (which was not certified by peer review) is the author/funder, who has granted bioRxiv a license to display the preprint in perpetuity. It is made available under aCC-BY 4.0 International license.

1195 than *E. coli* LPS, although the difference is weaker for donor s. *B. theta* 4PP LPS elicits weaker
1196 upregulation of genes than *B. theta* WT LPS. Data represent means obtained from three
1197 independent treatment replicates for each treatment and donor. Lines denote fit from a linear
1198 regression, with slope indicated.

bioRxiv preprint doi: https://doi.org/10.1101/2020.12.22.423985; this version posted December 22, 2020. The copyright holder for this preprint (which was not certified by peer review) is the author/funder, who has granted bioRxiv a license to display the preprint in perpetuity. It is made available under aCC-BY 4.0 International license.

Figure 2 - Figure Supplement 2

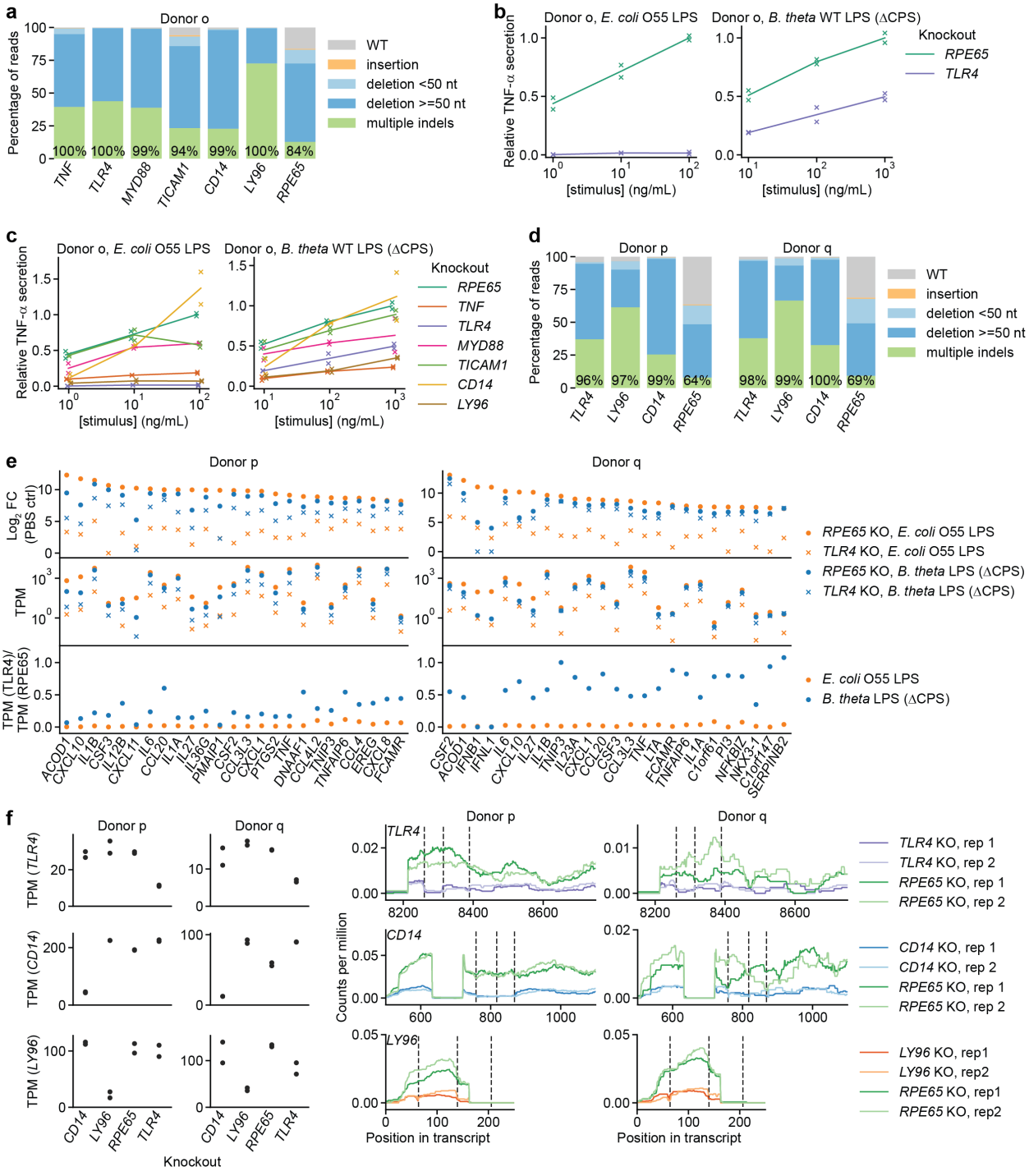

Figure 2 – Figure Supplement 2. *TLR4* knockout does not completely eliminate the response to *B. theta* LPS. **(a)** Percentage of genomic DNA reads assigned to different classes of outcomes after targeting each locus with multi-sgRNA Cas9 RNPs. Labeled values indicate total

bioRxiv preprint doi: https://doi.org/10.1101/2020.12.22.423985; this version posted December 22, 2020. The copyright holder for this preprint (which was not certified by peer review) is the author/funder, who has granted bioRxiv a license to display the preprint in perpetuity. It is made available under aCC-BY 4.0 International license.

1203 percentage of reads with a non-WT sequence. **(b)** Production of TNF-α by moDCs with
1204 knockout of *TLR4* or *RPE65* challenged with indicated concentrations of *E. coli* O55 LPS or *B.*
1205 *theta* LPS, normalized to cell counts and to TNF-α production by moDCs with knockout of
1206 *RPE65* and treated with the highest concentration of the respective LPS. Data represent two
1207 independent treatments, normalized to cell count obtained from replicate measurements. **(c)**
1208 Production of TNF-α by knockout moDCs, as in **(b)**, with data from additional knockouts also
1209 shown. All samples were treated with identical LPS concentrations, but x-values are slightly
1210 offset by sample for clarity. **(d)** Percentage of genomic DNA reads assigned to different classes
1211 of outcomes after targeting each locus with multi-sgRNA Cas9 RNPs. Labeled values indicate
1212 total percentage of reads with a non-WT sequence. **(e)** Expression levels of selected genes after
1213 stimulation of knockout moDCs from two donors with 3 ng/mL *E. coli* O55 LPS and 100 ng/mL
1214 *B. theta* WT LPS (donor p) or 10 ng/mL *E. coli* O55 LPS and 30 ng/mL *B. theta* WT LPS (donor
1215 q). Treatment concentrations were chosen based on similar transcriptional upregulation observed
1216 by qPCR (Figure 2 – Figure Supplement 1b). Log_2 fold-changes compared to control cells (PBS-
1217 treated, knockout of *RPE65*), transcript counts per million (TPM), or the ratio of TPM in moDCs
1218 with knockout of *TLR4* and moDCs with knockout of *RPE65* are shown for the 25 genes with the
1219 largest summed log_2 fold-changes after treatment with *E. coli* O55 LPS and *B. theta* WT LPS in
1220 moDCs with knockout of *RPE65*. MoDCs with *TLR4* knockout exhibit almost no transcriptional
1221 changes in response to *E. coli* LPS but upregulate many genes in response to *B. theta* WT LPS,
1222 with the exception of genes downstream of TRIF, such as *IFNB1*. Data represent means obtained
1223 from two independent treatment replicates for each treatment and donor. **(f)** Assessment of
1224 transcript abundance for targeted genes in knockout moDC populations, revealing reduced
1225 transcript counts for targeted genes and further reduced mRNA coverage around sgRNA cut

bioRxiv preprint doi: https://doi.org/10.1101/2020.12.22.423985; this version posted December 22, 2020. The copyright holder for this preprint (which was not certified by peer review) is the author/funder, who has granted bioRxiv a license to display the preprint in perpetuity. It is made available under aCC-BY 4.0 International license.

1226 sites. Left: Transcript counts (transcripts per million) for targeted genes in different PBS-treated
1227 (control) knockout moDC populations. Data represent measurements from independent
1228 replicates. Right: Transcript read coverage for targeted genes in different PBS-treated (control)
1229 knockout moDC populations. sgRNA cut sites are indicated by vertical dashed lines. Only exons
1230 with the sgRNA cut sites are shown.
1231
1232

bioRxiv preprint doi: https://doi.org/10.1101/2020.12.22.423985; this version posted December 22, 2020. The copyright holder for this preprint (which was not certified by peer review) is the author/funder, who has granted bioRxiv a license to display the preprint in perpetuity. It is made available under aCC-BY 4.0 International license.

Figure 3 - Figure Supplement 1

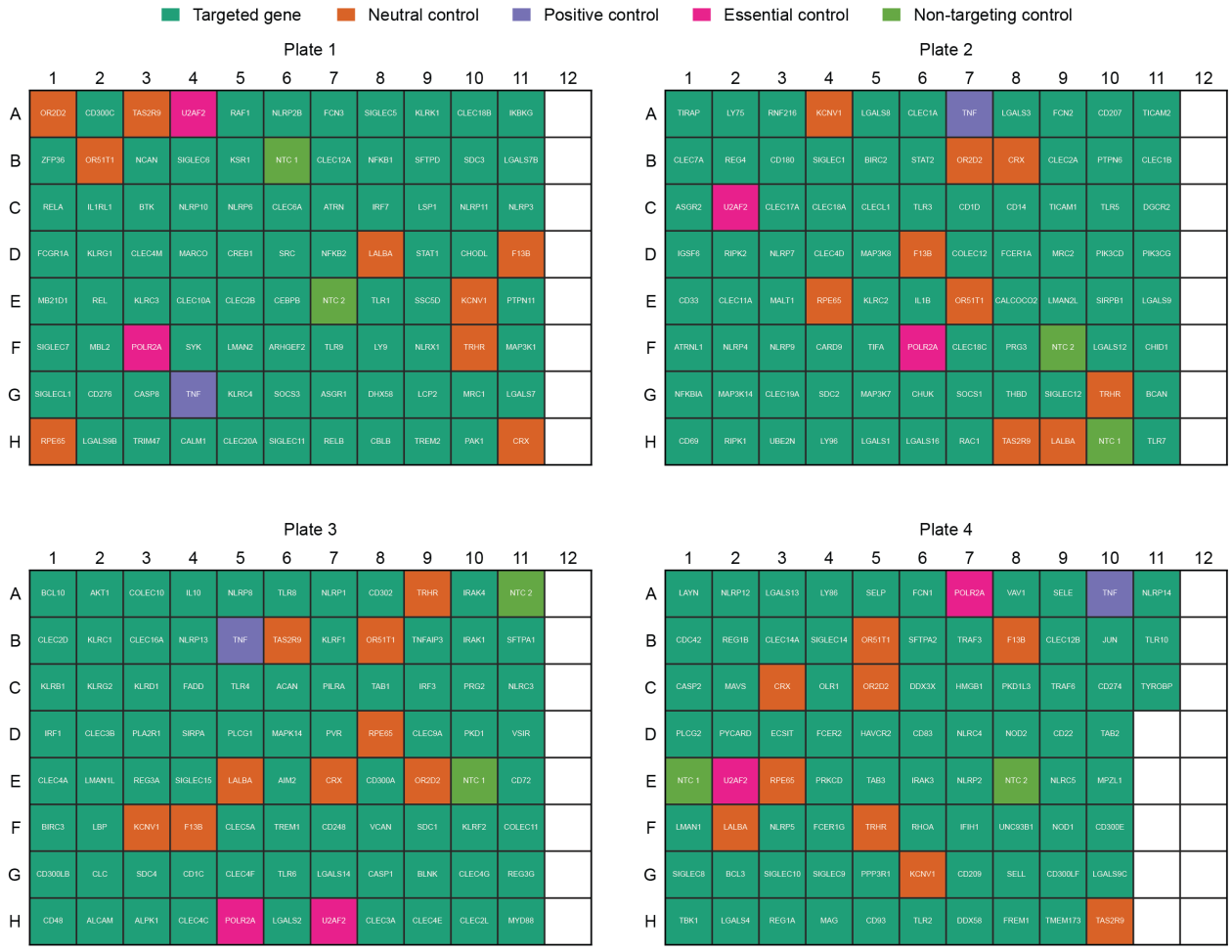

Figure 3 – Figure Supplement 1. Layout of sgRNAs in the arrayed genetic screen. Non-targeting controls and sgRNAs targeting neutral controls, essential controls, and *TNF* (positive control) were included on each plate in randomized positions.

bioRxiv preprint doi: https://doi.org/10.1101/2020.12.22.423985; this version posted December 22, 2020. The copyright holder for this preprint (which was not certified by peer review) is the author/funder, who has granted bioRxiv a license to display the preprint in perpetuity. It is made available under aCC-BY 4.0 International license.

Figure 3 - Figure Supplement 2

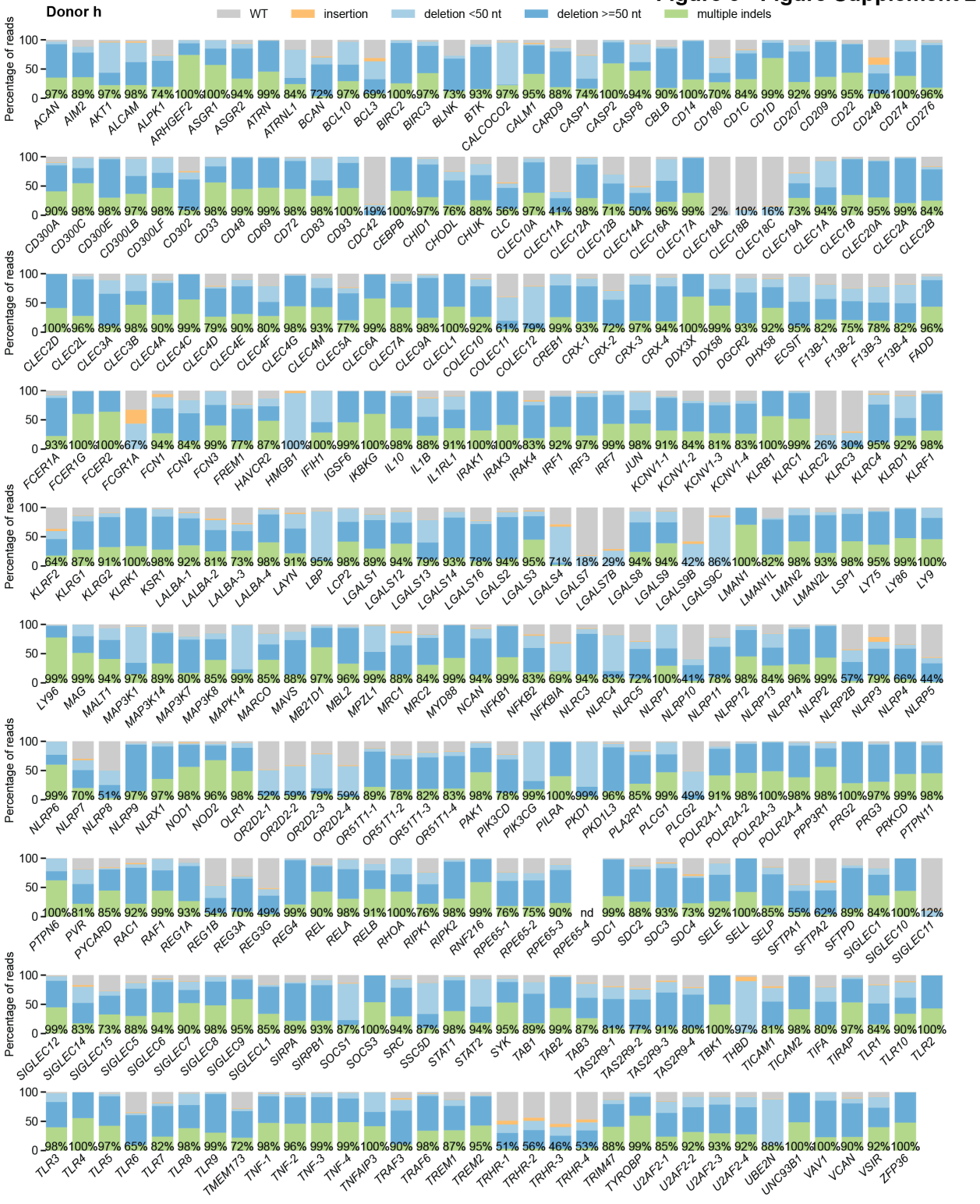

Figure 3 – Figure Supplement 2. Percentage of genomic DNA reads assigned to different classes of outcomes after targeting each locus in the arrayed genetic screen (donor h). Labeled

bioRxiv preprint doi: https://doi.org/10.1101/2020.12.22.423985; this version posted December 22, 2020. The copyright holder for this preprint (which was not certified by peer review) is the author/funder, who has granted bioRxiv a license to display the preprint in perpetuity. It is made available under aCC-BY 4.0 International license.

values indicate total percentage of on-target reads with a non-WT sequence. For loci with percentages labeled as "nd", sequencing library preparation failed and editing efficiency was not quantified. For genes targeted on each plate, editing efficiency was estimated for each plate individually. Loci are denoted as *locus*-# with # indicating the plate number.

bioRxiv preprint doi: https://doi.org/10.1101/2020.12.22.423985; this version posted December 22, 2020. The copyright holder for this preprint (which was not certified by peer review) is the author/funder, who has granted bioRxiv a license to display the preprint in perpetuity. It is made available under aCC-BY 4.0 International license.

Figure 3 - Figure Supplement 3

Figure 3 – Figure Supplement 3. Percentage of genomic DNA reads assigned to different classes of outcomes after targeting each locus in the arrayed genetic screen (donor i). Labeled

bioRxiv preprint doi: https://doi.org/10.1101/2020.12.22.423985; this version posted December 22, 2020. The copyright holder for this preprint (which was not certified by peer review) is the author/funder, who has granted bioRxiv a license to display the preprint in perpetuity. It is made available under aCC-BY 4.0 International license.

values indicate total percentage of on-target reads with a non-WT sequence. For loci with percentages labeled as "nd", sequencing library preparation failed and editing efficiency was not quantified. For genes targeted on each plate, editing efficiency was estimated for each plate individually. Loci are denoted as *locus*-# with # indicating the plate number.

bioRxiv preprint doi: https://doi.org/10.1101/2020.12.22.423985; this version posted December 22, 2020. The copyright holder for this preprint (which was not certified by peer review) is the author/funder, who has granted bioRxiv a license to display the preprint in perpetuity. It is made available under aCC-BY 4.0 International license.

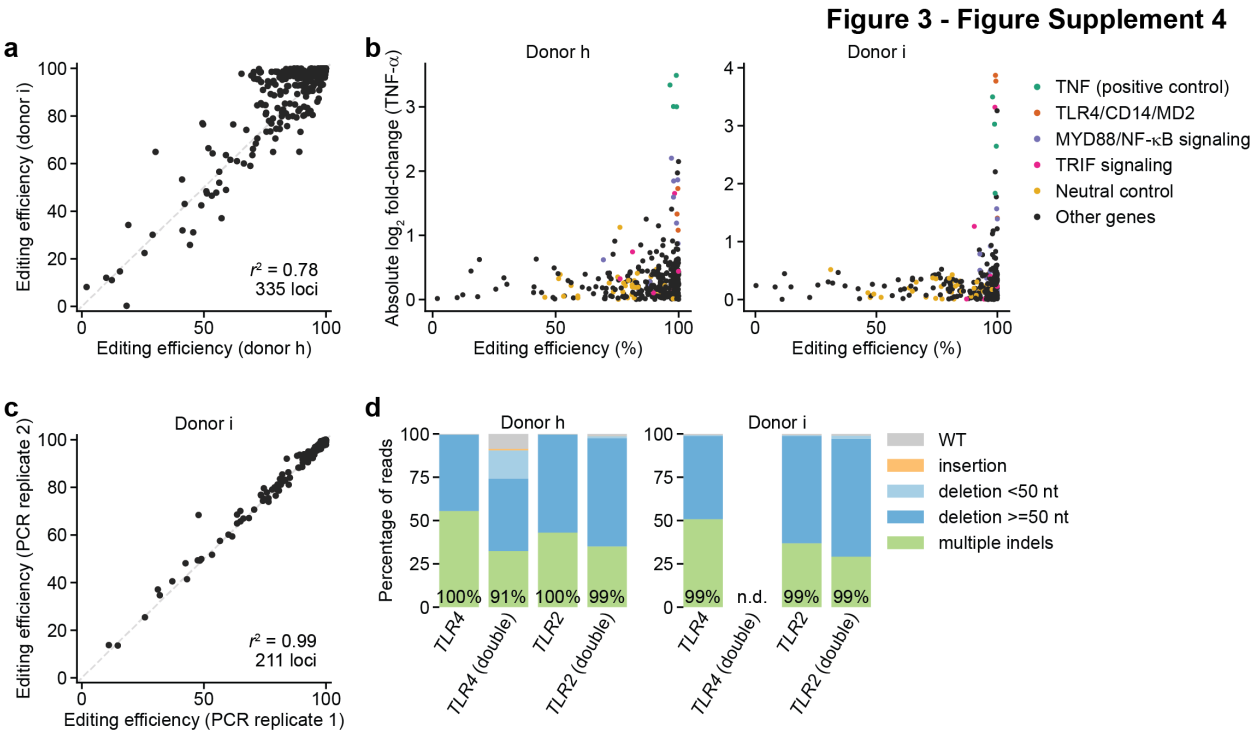

Figure 3 – Figure Supplement 4. Further analysis of editing outcomes from genetic screens. **(a)** Comparison of editing efficiencies observed in two independent donors for 335 loci. r^2 denotes squared Pearson correlation. **(b)** Comparison of screen phenotype (absolute value of $\log_2$ fold-change in TNF-α secretion after stimulation with *B. theta* LPS, mean of two treatment replicates) and editing efficiency, suggesting that high editing efficiency is required for a strong screen phenotype. **(c)** Comparison of editing efficiencies observed for two sequencing libraries prepared and sequenced independently, suggesting that the sequencing library preparation protocol and correction for size bias result in reproducible editing efficiencies. The second replicate was only performed for 211 loci. **(d)** Percentage of genomic DNA reads assigned to different classes of outcomes after targeting indicated loci with Cas9 RNPs. Labeled values indicate total percentage of reads with a non-WT sequence. For donor i, editing efficiency at the *TLR4* locus was not determined for the cell population simultaneously electroporated with Cas9 RNPs targeting *TLR4* and *TLR2*.

bioRxiv preprint doi: https://doi.org/10.1101/2020.12.22.423985; this version posted December 22, 2020. The copyright holder for this preprint (which was not certified by peer review) is the author/funder, who has granted bioRxiv a license to display the preprint in perpetuity. It is made available under aCC-BY 4.0 International license.

Figure 3 - Figure Supplement 5

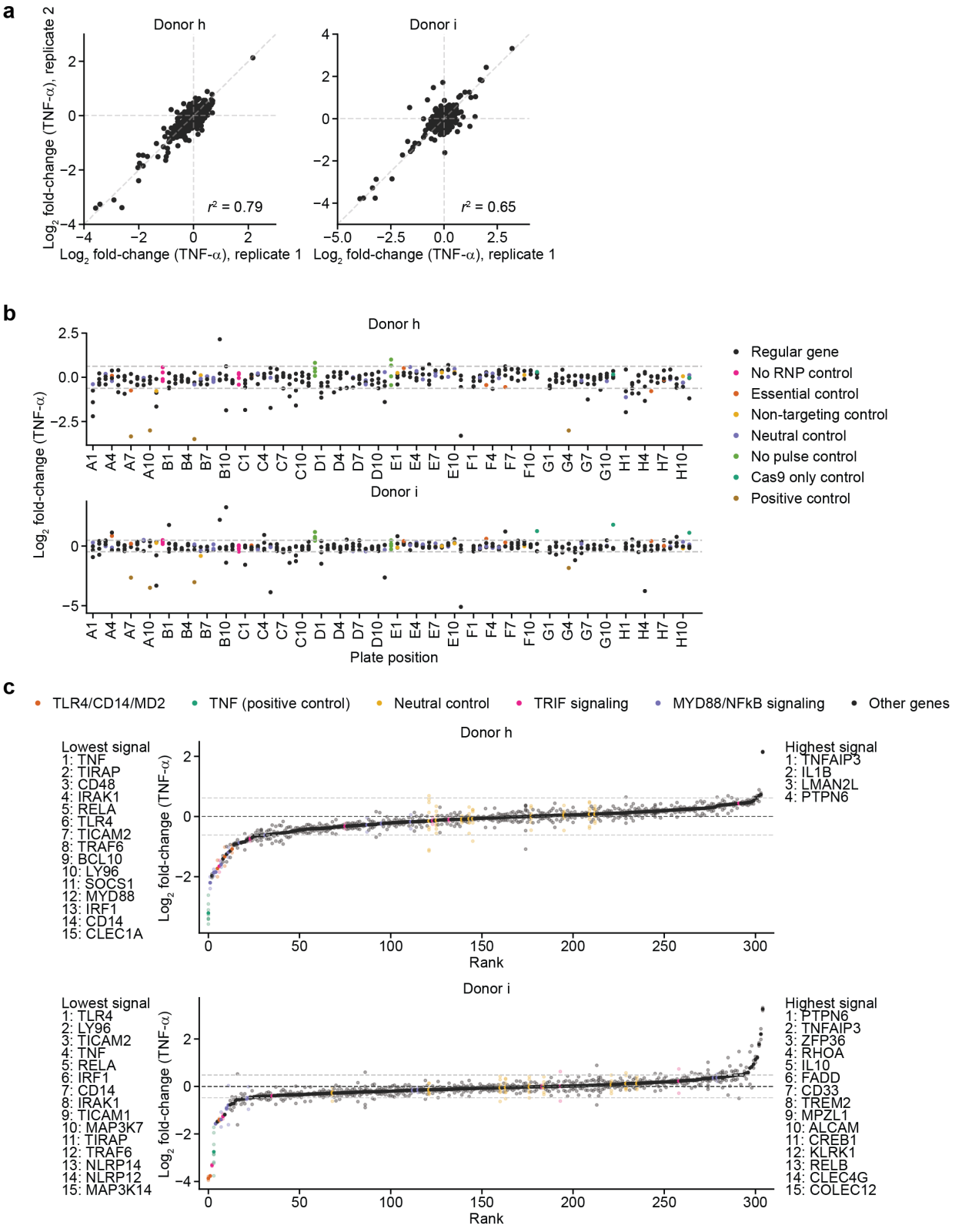

1271

bioRxiv preprint doi: https://doi.org/10.1101/2020.12.22.423985; this version posted December 22, 2020. The copyright holder for this preprint (which was not certified by peer review) is the author/funder, who has granted bioRxiv a license to display the preprint in perpetuity. It is made available under aCC-BY 4.0 International license.

Figure 3 – Figure Supplement 5. Screen phenotypes. **(a)** Comparison of phenotypes derived from replicate treatments for each donor. Each data point represents data from a single treatment replicate and two cell count replicates. r^2 denotes squared Pearson correlation. **(b)** Screen phenotypes ($\log_2$ fold-changes in TNF-α secretion relative to neutral controls) stratified by plate position. Each data point represents the average of two replicate treatments and two cell count replicates. Horizontal dashed lines denote 2 standard deviations of the phenotypes from all neutral gene controls. **(c)** Screen phenotypes (log2 fold-changes in TNF-α secretion) ordered by magnitude. Solid points represent the average of all replicate treatments; lower saturation points represent individual treatment measurements. Horizontal dashed lines denote 2 standard deviations of the phenotypes from all neutral gene controls. Up to 15 genes with the strongest phenotypes greater than 2 standard deviations (neutral gene controls) in either direction are listed.

bioRxiv preprint doi: https://doi.org/10.1101/2020.12.22.423985; this version posted December 22, 2020. The copyright holder for this preprint (which was not certified by peer review) is the author/funder, who has granted bioRxiv a license to display the preprint in perpetuity. It is made available under aCC-BY 4.0 International license.

Figure 3 - Figure Supplement 6

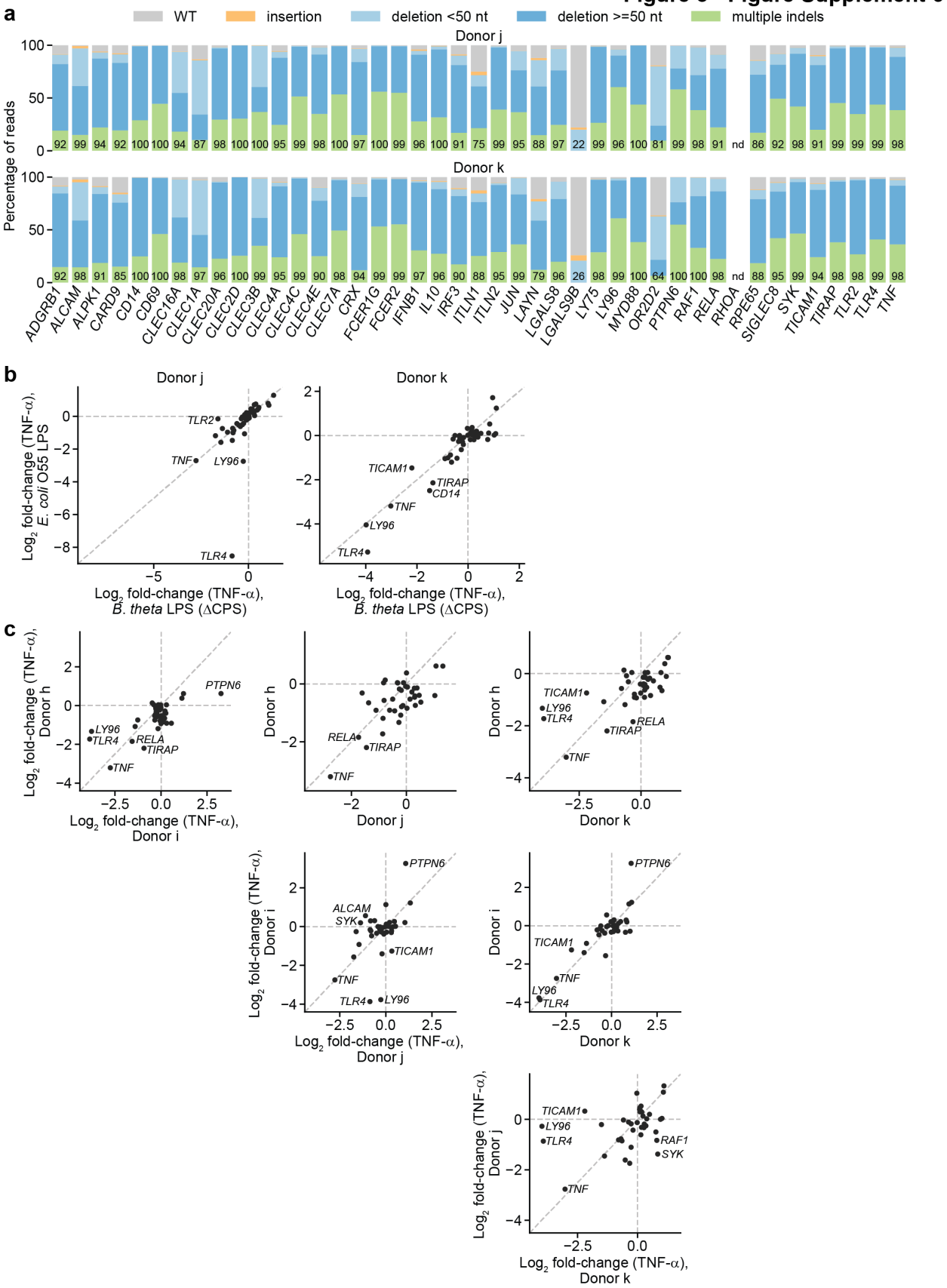

1286

bioRxiv preprint doi: https://doi.org/10.1101/2020.12.22.423985; this version posted December 22, 2020. The copyright holder for this preprint (which was not certified by peer review) is the author/funder, who has granted bioRxiv a license to display the preprint in perpetuity. It is made available under aCC-BY 4.0 International license.

Figure 3 – Figure Supplement 6. Validation of screen results in moDCs from two additional, independent donors. **(a)** Percentage of genomic DNA reads assigned to different classes of outcomes after targeting indicated loci in cells from two independent donors. Labeled values indicate total percentage of reads with a non-WT sequence. Editing efficiency was not quantified for *RHOA*. **(b)** Log_2 fold-change in TNF-α production by knockout moDCs challenged with 10 ng/mL *E. coli* O55 LPS or 100 ng/mL *B. theta* LPS relative to production in moDCs with knockout of neutral genes, normalized to cell counts. For donor j, knockout of *TLR2* decreased the response to *B. theta* LPS but not *E. coli* LPS. Other genes with large log_2 fold-changes are also labeled. Each data point represents data from two treatment replicates and a single cell count measurement. **(c)** Log_2 fold-change in TNF-α production by knockout moDCs challenged with 100 ng/mL *B. theta* LPS from 4 independent donors, relative to production in moDCs with knockout of neutral genes. Data for donors h and i are derived from the arrayed screen. Genes with $|log_2 \text{ fold-change}| > 1.8$ or $\Delta log_2 \text{ fold change} > 1.3$ are labeled.

bioRxiv preprint doi: https://doi.org/10.1101/2020.12.22.423985; this version posted December 22, 2020. The copyright holder for this preprint (which was not certified by peer review) is the author/funder, who has granted bioRxiv a license to display the preprint in perpetuity. It is made available under aCC-BY 4.0 International license.

Supplemental File Legends

Supplementary File 1. Sequences of sgRNAs and amplicon PCR primers used in this work, including details on sgRNA binding sites.

Supplementary File 2. Counts corresponding to different outcomes, corrected for amplicon size, after amplicon sequencing for all donors except donors h and i.

Supplementary File 3. Raw and processed TNF-α and IL-10 ELISA and cell count data for the genetic screens.

Supplementary File 4. Counts corresponding to different outcomes, corrected for amplicon size, after amplicon sequencing for donors h and i.